The Astrophysical Journal, 855:66 (19pp), 2018 March 1 https://doi.org/10.3847/1538-4357/aaab5b

Color Variabilities of Spectrally Defined Red QSOs at $z = 0.3$–1.2

I-Chenn Chen[1], Chorng-Yuan Hwang[1], Nick Kaiser[2], Eugene A. Magnier[2], Nigel Metcalfe[3], and Christopher Waters[2]
[1] Graduate Institute of Astronomy, National Central University, Chung-Li 32054, Taiwan; m949011@astro.ncu.edu.tw
[2] Institute for Astronomy, University of Hawaii at Manoa, Honolulu, HI 96822, USA
[3] Department of Physics, Durham University, South Road, Durham DH1 3LE, UK

Received 2016 January 19; revised 2018 January 24; accepted 2018 January 25; published 2018 March 8

Abstract

We study the brightness and the color variabilities of 34 red and 122 typical quasi-stellar objects (QSOs) at $z = 0.3$–1.2 using data from the Pan-STARRS Medium Deep Survey. The red and the typical QSOs are selected based on the ratios of the flux densities at 3000 Å to those at 4000 Å in the rest frame. We find that 16 out of 34 red QSOs are identified as extended sources, which exhibit strong brightness and color variabilities at shorter wavelengths due to the contamination of the emission from their host galaxies. Some point-like QSOs with significant color variabilities are able to change their color classification according to our spectral definition. The timescales of the color variabilities for these point-like QSOs are within 4 years, suggesting that the size scales of the mechanisms producing the color variabilities are less than a few light years. The spectra of some extended and point-like red QSOs can be well fitted with the dust-reddened spectra of a typical QSO, while others are difficult to explain with dust reddening.

Key words: galaxies: active – galaxies: nuclei – quasars: general

1. Introduction

Quasi-stellar objects (QSOs) are among the most powerful celestial objects in the universe (Matthews & Sandage 1963; Schmidt 1963). A QSO is defined to be an extremely luminous active galactic nucleus (AGN) lying in the center of a host galaxy with a super massive black hole being fed with material from a surrounding accretion disk, which is surrounded by a dusty torus (Antonucci 1993; Urry & Padovani 1995). A QSO may show different spectral properties with different viewing angle. Emission from the central regions of the QSOs can be obscured by the torus if the viewing angle is in the edge-on direction of the torus. A QSO observed from this edge-on line of sight are called type-2 QSO.

The spectrum of a typical QSO exhibits prominent broad lines and narrow lines overlying a non-stellar continuum, which peaks in the near-UV waveband in the rest frame (Vanden Berk et al. 2001; Walcher et al. 2011, and reference therein). The relatively strong near-UV emission makes QSOs optically blue objects (Shields 1978; Malkan & Sargent 1982). Nevertheless, several studies have suggested the existence of a population of red QSOs. Most studies interpreted the atypical redness in terms of dust obscuration (Webster et al. 1995; Richards et al. 2003; Glikman et al. 2004, 2007; Urrutia et al. 2009; Glikman et al. 2012; Fynbo et al. 2013; Glikman et al. 2013). We note that the red QSOs cannot be explained as a type-2 QSOs because the red QSOs show broad emission lines that must originate in the central region of the QSOs inside the torus. In fact, a merger-driven QSO/galaxy co-evolution scenario has been suggested to explain red QSOs as QSOs in a growing phase, enshrouded by dust from the merging host galaxies, and the red QSOs will eventually evolve to become "typical" blue QSOs (Sanders et al. 1988; Glikman et al. 2012).

Several scenarios other than dust reddening have also been proposed to explain this atypical redness. For example, red QSOs might have an intrinsic red continuum (Hall et al. 2006; Young et al. 2008) or red synchrotron emission turnover (Benn et al. 1998; Whiting et al. 2001), or they might be affected by infrared excess of the starlight from their host galaxies (Benn et al. 1998).

QSOs are well known for their non-periodic variability with timescales from days to years at almost all wavelengths (Ulrich et al. 1997; Vanden Berk et al. 2004). A rough "bluer-when-brighter" trend was found in most of these cases (Giveon et al. 1999; Vanden Berk et al. 2004; Wilhite et al. 2005; Sakata et al. 2011; Schmidt et al. 2012; Sun et al. 2014). Some studies (Cristiani et al. 1997; Giveon et al. 1999; Hawkins 2003; Vanden Berk et al. 2004) suggested that the optical variability of QSOs is wavelength dependent and that it generally displays larger variation amplitudes at shorter wavelengths. It is generally believed that optical variabilities are caused by accretion-disk instabilities (Rees 1984; Kawaguchi et al. 1998; Pereyra et al. 2006).

Despite a large number of studies on red QSOs, the criterion for defining a red QSO is still not well established. Most previous studies adopted photometric-color cuts to select their red QSO samples: Glikman et al. (2007, 2012) chose $R - K > 4$ and $J - K > 1.7$ color cuts as their red QSO selection criteria; Urrutia et al. (2009) and Glikman et al. (2013) made use of SDSS data and adopted r–$K > 5$ and $J - K > 1.5$ with $K < 17$ as their definition of red QSOs; and Fynbo et al. (2013) imposed $0.8 < g - r < 1.5$ and $r - i > 0.2$ as their selection criteria for their SDSS data. All these methods of defining the "redness" of QSOs are redshift dependent. We note that different criteria of selecting red QSOs might lead to different types of red QSOs; for example, the sources of Glikman et al. (2013) are highly reddened, whereas those of Fynbo et al. (2013) have relatively low levels of reddening. In addition to the non-uniformity between different selections, the photometric selection may also lead to some problematic issues, e.g., contamination from the redshifted emission lines.

Given the occurrence of color variability of QSO, it would be useful to know whether the existence of red QSO is related to color variability. Therefore, in this study, we classify our QSO samples with a redshift independent method using the

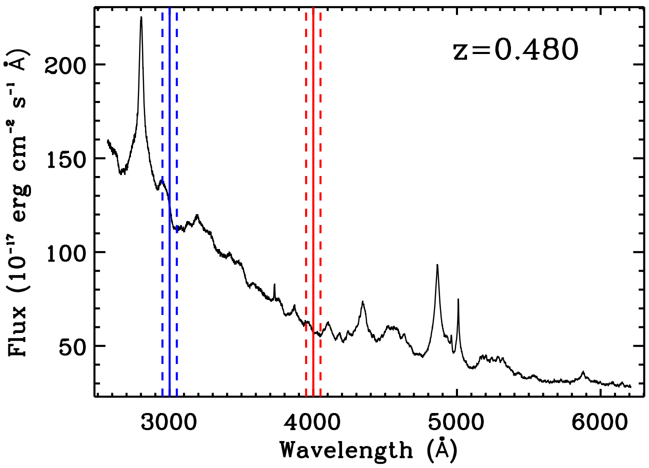

Figure 1. Rest-frame spectrum for one of our QSO sample, SDSS J000011.96+000225.2. We estimated the flux around 3000 Å (the blue solid line) and 4000 Å (the red solid line) by integrating the spectral regions from 2951 to 3050 Å (the two blue dashed lines) and the regions from 3951 to 4050 Å (the two red dashed lines).

SDSS spectra and study their color variabilities using the Pan-STARRS Medium Deep Survey (MDS). We describe the methodology for our QSO classification and data analysis in Sections 2 and 3, respectively. We present our results in Section 4 and discuss them in Section 5. Finally, we give our conclusions in Section 6. Throughout the paper, a flat cosmology is assumed with parameter value $\Omega_\Lambda = 0.7$, $\Omega_M = 0.3$, and $H_0 = 70\,\mathrm{km\,s^{-1}\,Mpc^{-1}}$. The AB magnitude system is used throughout unless stated otherwise.

2. Selection of Red QSOs

We selected our QSOs sample from the Quasar Catalog of SDSS Data Release 7 (DR7) (Schneider et al. 2010). There are 105,783 QSOs in the catalog. We defined red QSOs by estimating the ratios of their spectral flux densities at 3000 Å to those at 4000 Å in the rest frame using the SDSS spectral data (Figure 1). To ensure that spectral data around 3000 Å and 4000 Å in the rest frame are available in the SDSS spectra, we selected QSOs in a redshift region between $z = 0.3$ and 1.2. As a result, 32,296 QSOs were selected. We shifted the observed spectra to the rest frame according to the spectral redshifts and estimated the flux ratios using

$$\frac{f_{3000\,\text{Å}}}{f_{4000\,\text{Å}}} = \frac{\int_{2951\,\text{Å}}^{3050\,\text{Å}} f(\lambda)\,d\lambda}{\int_{3951\,\text{Å}}^{4050\,\text{Å}} f(\lambda)\,d\lambda}. \quad (1)$$

Figure 1 illustrates the wavelength regions for estimating the flux ratios. We then converted the flux ratios into magnitude differences like so:

$$m_{3000\,\text{Å}} - m_{4000\,\text{Å}} = -2.5 \times \log \frac{f_{3000\,\text{Å}}}{f_{4000\,\text{Å}}}. \quad (2)$$

In the left panel of Figure 2, we present the distribution of magnitude differences for the selected QSOs as function of their spectral redshifts obtained from the SDSS spectra. As $m_{3000\,\text{Å}} - m_{4000\,\text{Å}}$ is defined in the rest frame and is hence independent with redshift, its distribution remains similar at different redshifts. The histogram of $m_{3000\,\text{Å}} - m_{4000\,\text{Å}}$ is shown in the right panel of Figure 2. The distribution resembles a normal distribution with a peak at $m_{3000\,\text{Å}} - m_{4000\,\text{Å}} = -0.675$, but has an additional red tail. We fitted the left side of this distribution with a Gaussian curve and mirrored the curve to the right side to obtain a complete normal distribution. The standard deviation σ of this normal distribution is 0.11. We thus defined red QSOs as QSOs with magnitude differences, $m_{3000\,\text{Å}} - m_{4000\,\text{Å}}$, greater than 3σ away from the peak value ($m_{3000\,\text{Å}} - m_{4000\,\text{Å}} > -0.345$). For comparison, we also defined QSOs with magnitude differences within $\pm 1\sigma$ of the peak value ($-0.785 < m_{3000\,\text{Å}} - m_{4000\,\text{Å}} < -0.565$) as typical QSOs. With this selection, the extremely blue QSOs with $m_{3000\,\text{Å}} - m_{4000\,\text{Å}} < -0.785$ are not included in the classification of typical QSO. Ultimately, 18,282 typical QSOs and 2,458 red QSOs were selected. According to Schneider et al. (2010), 4392 quasars (4.15%) were classified as extended sources among the 105,783 quasars in the SDSS DR7 quasar catalog. We found that 400 typical QSOs (1.93%) and 322 red QSOs (1.55%) are classified as extended sources, while 17,882 typical QSOs (86.21%) and 2136 red QSOs (10.30%) are classified as point sources among the 20,740 QSOs we selected.

We investigated the variability of our selected QSOs using data from the MDS of the Panoramic Survey Telescope and Rapid Response System (PS1) (Kaiser et al. 2002, 2010; Hodapp et al. 2004; Chambers 2011). The MDS contains ten specific fields (Table 1). The filter system covers a spectral region between 4000 and 10500 Å and is separated into g_{P1}, r_{P1}, i_{P1}, z_{P1}, and y_{P1} bands (Tonry et al. 2012). PS1 uses the AB magnitude system, which is introduced by Oke & Gunn (1983) and was successfully applied to the SDSS (Fukugita et al. 1996). The MDS took images by cycling through these five bands over a four-days cycle; it took g_{P1} and r_{P1} band images on day 1; and then i_{P1}, z_{P1}, and y_{P1} band images on day 2, day 3, and day 4, respectively. The exposure times were 113 s for the g_{P1} and r_{P1} bands and 240 s for the i_{P1}, z_{P1}, and y_{P1} bands. The images of the MDS data were processed using the Pan-STARRS1 Image Processing Pipeline (IPP) (Magnier 2006, 2007; Magnier et al. 2008) and the photometric data were further calibrated with an uber-calibration-based technique (Schlafly et al. 2012). After cross-matching the selected QSOs with the objects detected from the MDS, we obtained 34 red QSOs (Table 6) and 122 typical QSOs (Table 7) located in the MDS fields.

We found that 16 of 34 red QSOs and eight of 122 typical QSOs are identified as extended sources by SDSS. When measuring the magnitudes of the “extended” QSOs, we noted that the measured magnitudes are related to the seeing of the observation if PSF magnitude is adopted. Therefore, we adopted the Kron magnitude and the PSF magnitude generated by IPP (Magnier et al. 2013) to acquire the apparent magnitudes of the “extended” QSOs and the point-like QSOs, respectively.

The MDS took eight images for a single field with the same filter on each observing night. We estimated the QSO’s magnitude of each night by averaging the photometric measurements of the night. To do this, we first rejected the outliers of the eight measurements. Photometric measurements are regarded as outliers if the differences between the measurements and the median magnitude are greater than 3σ. We then estimated the mean of the remaining measurements and computed the standard errors. We rejected the data with

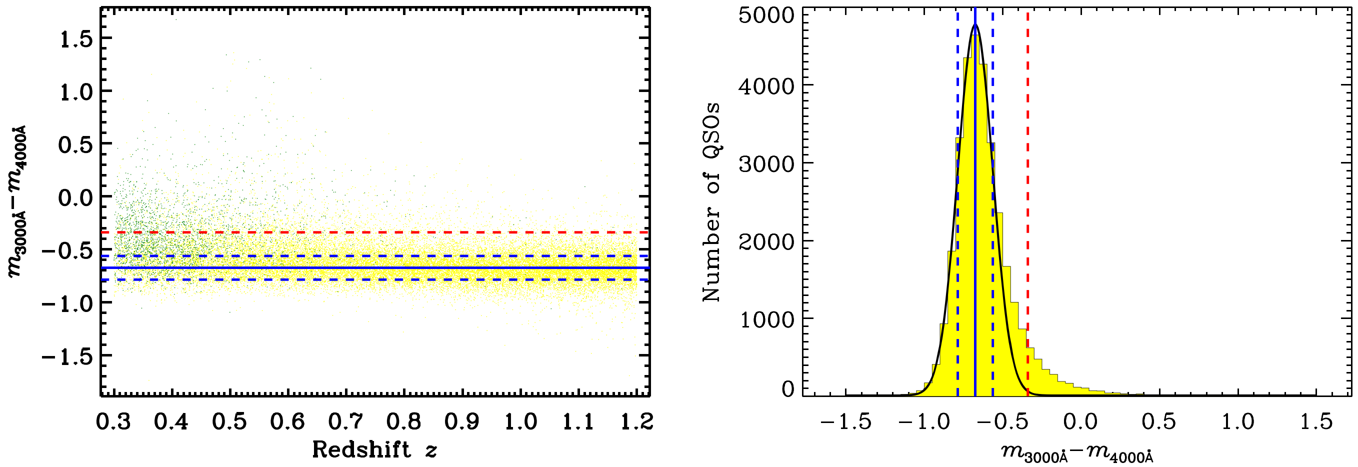

Figure 2. Left panel: distribution of magnitude difference, $m_{3000\ Å}-m_{4000\ Å}$, as a function of redshift; the yellow dots represent point-like QSOs while green dots present extended QSOs. Right panel: histogram of $m_{3000\ Å}-m_{4000\ Å}$ with a 0.05 bin size. The black curve in the right panel is a Gaussian curve with a peak located at −0.675, which we mark with solid blue lines in both panels. The dashed blue lines mark the 1σ standard deviation of this Gaussian curve. The red dashed lines mark the value of −0.345, which is the value 3σ greater than the central peak. We adopt this value as the lower limit of defining red QSOs.

Table 1
Information of PS1 MDS Fields

MD Field	R.A.(J2000)	Decl.(J2000)
MD01	02 : 23 : 30	−04 : 15 : 00
MD02	03 : 32 : 24	−27 : 48 : 00
MD03	08 : 42 : 22	+44 : 19 : 00
MD04	10 : 00 : 00	+02 : 12 : 00
MD05	10 : 47 : 40	+58 : 05 : 00
MD06	12 : 20 : 00	+47 : 07 : 00
MD07	14 : 14 : 49	+53 : 05 : 00
MD08	16 : 11 : 09	+54 : 57 : 00
MD09	22 : 16 : 45	+00 : 17 : 00
MD10	23 : 29 : 15	−00 : 26: 00

Note. MD field: field ID; R.A.: right ascension; decl.: declination.

less than four measurements in a night. We also rejected the data that have errors larger than 3σ of the error distribution.

3. Data Analysis

To quantify the brightness variation of a QSO, we estimated the brightness variability amplitude (hereafter, BVA), $\sigma_{\rm rms}$, of the observed magnitudes for each QSO (Yip et al. 2009; Ai et al. 2010; Zuo et al. 2012):

$$\sigma_{\rm rms} = \sqrt{\Sigma^2 - \xi^2}, \tag{3}$$

where

$$\Sigma^2 = \frac{1}{N-1}\sum_{j=1}^{N}(X_j - \mu)^2, \tag{4}$$

$$\xi^2 = \frac{1}{N}\sum_{j=1}^{N}\sigma_j^2, \tag{5}$$

N is the number of observations for a single QSO in each filter band, X_j is the magnitude measured from the jth observation, σ_j is the photometric error of the jth magnitude, and μ is the mean magnitude. If $\Sigma \leqslant \xi$, $\sigma_{\rm rms}$ is regarded as zero.

To estimate the colors of the QSOs, we interpolated the observed light curves of two individual filters onto a common time sampling. We removed the data points occurring at the edges of each observational season to make sure that all the interpolated points are generated with their neighboring points within the same observational season. The corresponding error is also estimated through error propagation calculation and the error of the interpolated data point is the mean of the errors of its neighboring points. We then calculated the colors for a common time. Figure 3 presents the interpolated light curves of SDSS J083732.19+450139.7 for each band. We also adopted the $\sigma_{\rm rms}$ value defined above to quantify the color variability amplitude (hereafter, CVA) of the QSOs.

We measured the luminosity of our selected QSOs by estimating their rest-frame fluxes at 4100 Å:

$$f_{4100\ Å} = \frac{1}{100} \times \int_{4051\ Å}^{4150\ Å} f(\lambda)\, d\lambda. \tag{6}$$

We obtained the absolute magnitudes of the QSOs at 4100 Å, $M_{4100\ Å}$, using the fluxes and luminosity distances derived from the spectral redshifts.

4. Results

4.1. Brightness Variability

Figure 4 shows the distributions of the BVAs for the red and the typical QSOs as a function of their redshifts. We note that most of our selected red QSOs occur at low redshifts, whereas the typical QSOs are uniformly distributed over the entire range of redshift. To investigate the origin of this distribution, we plotted the BVAs as a function of the absolute magnitudes, $M_{4100\ Å}$, of the QSOs in Figure 5, which shows that the majority of red QSOs are less luminous than their typical counterparts, hence they are less likely to be observed in high-redshift region. In fact, the majority of QSOs detected at low redshifts are less luminous than those at high redshifts (Figure 6). This phenomenon is due to the Malmquist bias; that is, the observer can only detect luminous objects at greater distance.

The mean values of the BVAs for the typical and the red QSOs are shown in Table 2. We also present the p-values in the Kolmogorov–Smirnov (K–S) statistics of the BVAs between the red QSOs and the typical QSOs in Table 2. The p-values of the BVAs are 0.677, 0.893, 0.077, and 0.260 in g_{P1}, r_{P1}, i_{P1},

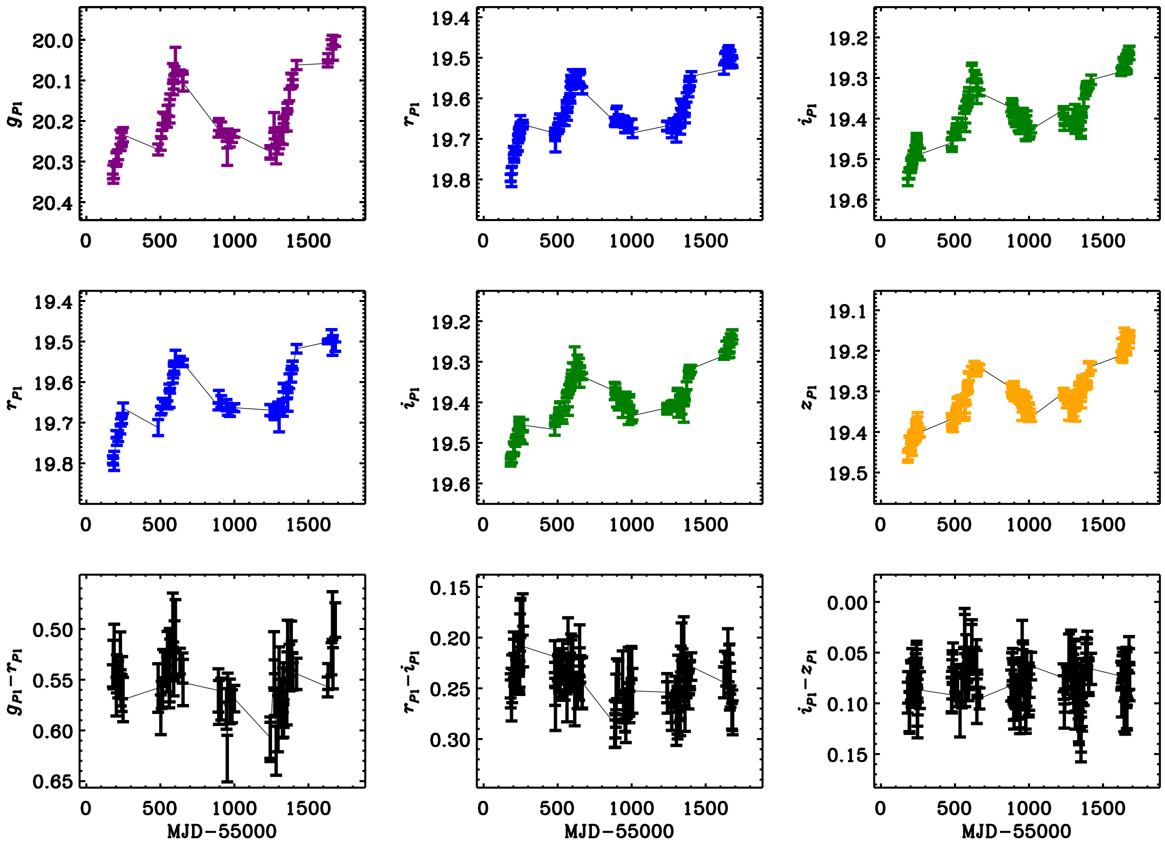

Figure 3. Light curves and the color variabilities of SDSS J083732.19+450139.7. The left column shows the light curves in g_{P1} and r_{P1} bands, and the $g_{P1}-r_{P1}$ color variabilities; the middle column shows the light curves in r_{P1} and i_{P1} bands and the $r_{P1}-i_{P1}$ color variabilities; and the right column shows the light curves in i_{P1} and z_{P1} bands, and the $i_{P1}-z_{P1}$ color variabilities.

and z_{P1} bands, respectively, suggesting that the distributions of the BVAs for the whole sample of the red and the typical QSOs are indistinguishable, except for the result of i_{P1} band since the p-value is less than 0.1. The p-values for the point-like QSOs are also shown in Table 2, which are 0.851, 0.962, 0.364 and 0.349 in g_{P1}, r_{P1}, i_{P1} and z_{P1} bands, respectively, suggesting that the distributions of the BVAs for the point-like red QSOs and the point-like typical QSOs are also indistinguishable.

Most of the extended QSOs (14 of 16 red QSOs and six of eight typical QSOs) are located at low redshifts ($z < 0.6$), and are hence less luminous ($M_{4100\,\text{Å}} > -24$; Figure 6). We note that the extended QSOs are more variable at shorter wavelengths than at longer wavelengths (Table 2); the mean BVAs of the extended typical QSOs decrease from 0.2022 in g_{P1} band to 0.0863 in z_{P1} band with a two-sample t-test probability $p = 3.89 \times 10^{-4}$, and those of the extended red QSOs decrease from 0.1350 in g_{P1} band to 0.0579 in z_{P1} band with a two-sample t-test probability $p = 2.99 \times 10^{-4}$.

4.2. Color Variability

The mean CVAs for the typical and the red QSOs are shown in Table 3. We also show the p-values in the K–S statistics of the CVAs between the red and the typical QSOs in Table 3. These results suggest that the distributions of the CVAs for the red and the typical QSOs are very different. Furthermore, the red QSOs are more color variable at short wavelengths than at long wavelengths; the mean CVA decreases from 0.0403 in $g_{P1} - r_{P1}$ to 0.0286 in $i_{P1} - z_{P1}$ with a two-sample t-test probability $p = 0.043$ between these two colors; on the other hand, the mean CVAs of the typical QSOs remains almost constant with a value of 0.0253 in $g_{P1}-r_{P1}$ and 0.0243 in $i_{P1}-z_{P1}$, and the two-sample t-test probability is $p = 0.645$ between these two colors.

Figure 7 shows the distributions of the CVAs for the red and the typical QSOs as a function of their redshifts. The mean values of the CVAs for the red and the typical QSOs with redshift less than 0.6 are shown in Table 3. We also show the p-values of the K–S statistics of the CVAs in Table 3. Figure 8 shows the distributions of the CVAs as a function of absolute magnitudes $M_{4100\,\text{Å}}$. The mean values of the CVAs for the typical and the red QSOs with $M_{4100\,\text{Å}}$ fainter than −24 are shown in Table 3. We also show the p-values of the K–S statistics for the distributions of the CVAs between the typical and the red QSOs in Table 3.

We find that most of the low-redshift red QSOs are extended sources. The mean values of the CVAs for both the extended and the point-like QSOs are shown in Table 3. The extended QSOs, whether red or typical, are more variable than the point-like QSOs at short wavelengths; the mean $g_{P1}-r_{P1}$ CVA of the extended typical QSOs (0.0643) is much greater than that of the point-like typical QSOs (0.0225) with a two-sample t-test probability $p = 6.24 \times 10^{-11}$; the mean $g_{P1}-r_{P1}$ CVA of the extended red QSOs (0.0516) is also greater than that of the point-like red QSOs (0.0302) with a two-sample t-test probability $p = 0.020$. The CVAs for the extended sources exhibit an apparent decrease with increasing wavelengths; the mean CVAs of the extended typical QSOs decrease from 0.0643 in $g_{P1}-r_{P1}$ to 0.0285 in $i_{P1}-z_{P1}$ with a two-sample t-test probability $p = 0.030$; similarly, the mean CVAs of the

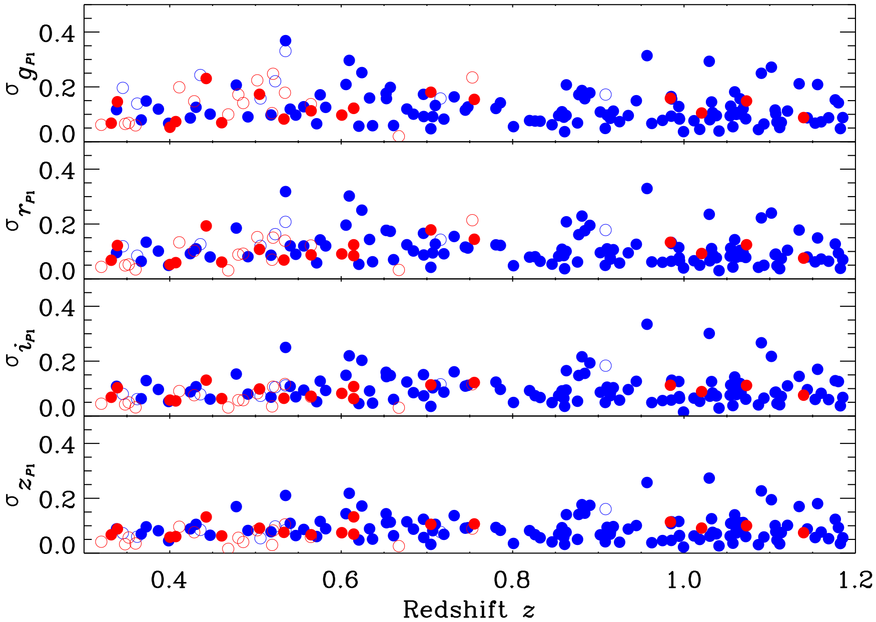

Figure 4. Distributions of the BVAs of the red and the typical QSOs as a function of redshifts in g_{P1}, r_{P1}, i_{P1}, and z_{P1} bands (from top to bottom), respectively. The red symbols represent red QSOs, while the blue symbols represent the typical QSOs. The filled circles represent the SDSS-identified point sources, while the open circles represent the SDSS-identified extended sources.

extended red QSOs decrease from 0.0516 in $g_{P1}-r_{P1}$ to 0.0181 in $i_{P1}-z_{P1}$ with a two-sample t-test probability $p = 0.001$.

The mean CVAs and the K–S statistics between the point-like red QSOs and the point-like typical QSOs are shown in Table 3. The K–S statistics indicate that the CVAs distributions between the point-like red QSO and the point-like typical QSOs are different. The mean CVAs also indicate that the point-like red QSOs are more color variable than the the point-like typical QSOs, with t-test probabilities $p =$ 0.029, 0.002, and 0.004 in $g_{P1}-r_{P1}$, $r_{P1}-i_{P1}$ and $i_{P1}-z_{P1}$. Nevertheless, for the low-redshift QSOs ($z < 0.6$), we find that the distributions of the point-like red QSOs and the point-like typical QSOs are indistinguishable (Table 3).

We present the correlations between the BVAs and the CVAs in Figure 9. The Pearson correlation coefficients and the p-values of the two-sided t-test are presented in Table 4. The results suggest that the BVAs and the CVAs are correlated, except for the results of $\sigma_{r_{P1}}$ versus $\sigma_{g_{P1}-r_{P1}}$ for the red QSOs, which is not significant. We also show the results for the point-like QSOs in Table 4, which suggest the BVAs and the CVAs for point-like QSOs are also correlated, except for the results of $\sigma_{i_{P1}}$ versus $\sigma_{i_{P1}-z_{P1}}$ and $\sigma_{z_{P1}}$ versus $\sigma_{i_{P1}-z_{P1}}$ for the red QSOs, which the are not significant.

5. Discussion

Most previous studies classified their QSO samples using photometric-color-based methods (Glikman et al. 2007; Urrutia et al. 2009; Fynbo et al. 2013). Red QSOs with different redshifts would be classified with different color criteria using these methods. Our method instead classifies QSOs based on the rest-frame flux ratios obtained from spectra. We compare the same spectral regions in the rest frame and avoid the contamination from emission lines, such as [Mg II], [O II], H γ, and [Fe II]. Besides, we note that different color criteria of selecting red QSOs might lead to different types of red QSOs. Therefore, the red QSOs obtained using our definition may be different from those found in previous studies.

We find that there is a large fraction of red QSOs (16 of 34) exhibiting extended morphologies. These "extended" red QSOs are obviously more variable than other QSOs at low wavelengths. Most of our selected red QSOs occur at low redshift, and appear to be fainter than the typical QSOs (see Figure 6), suggesting that the observed spectra of these low-redshift red QSOs might be strongly affected by their host galaxies. However, we note that there may be at least two different types of red QSOs; our high-redshift red QSOs are as bright as the typical QSOs and have less color variabilities than the low-redshift red QSOs as shown in Figure 7. This observation suggests that there may be several possible mechanisms for the origin of red QSOs.

Many extended QSOs in our samples exhibit significant color variabilities at short wavelengths. Nevertheless, some point-like QSOs also have considerable CVAs, such as SDSS J095823.73+011235.7, which is a point-like red QSO. The CVAs of SDSS J095823.73+011235.7 are 0.068, 0.049 and 0.056 in $g_{P1}-r_{P1}$, $r_{P1}-i_{P1}$ and $i_{P1}-z_{P1}$, respectively; besides, the $g_{P1}-r_{P1}$ vary between 0.240 and 0.509 in the color light curve of SDSS J095823.73+011235.7. We note that the Pan-STARRS magnitudes are measured in AB magnitude system. If we convert the Pan-STARRS magnitudes to a magnitude system using flux per wavelength, i.e., the ST system, the minimum and the maximum $g_{P1}-r_{P1}$ colors of SDSS J095823.73+011235.7 become −0.385 and −0.116. Considering the redshift of SDSS J095823.73+011235.7 ($z = 0.505$), the $g_{P1}-r_{P1}$ color is similar to the rest frame $m_{3000\,\text{Å}} - m_{4000\,\text{Å}}$. The original color of SDSS J095823.73+011235.7 is −0.278 from our spectral definition. Thus, it is possible for SDSS J095823.73+011235.7 to move out of the region of our red QSOs ($m_{3000\,\text{Å}} - m_{4000\,\text{Å}} > -0.345$) or to become extremely red. Similarly, we find that SDSS J233029.16+003746.5, a point-like typical QSO with $z = 0.535$, show $g_{P1} - r_{P1}$ color variability between −0.771 and −0.418 in the ST magnitude system. The color $g_{P1}-r_{P1}$ is also similar to the rest frame $m_{3000\,\text{Å}} - m_{4000\,\text{Å}}$. The original

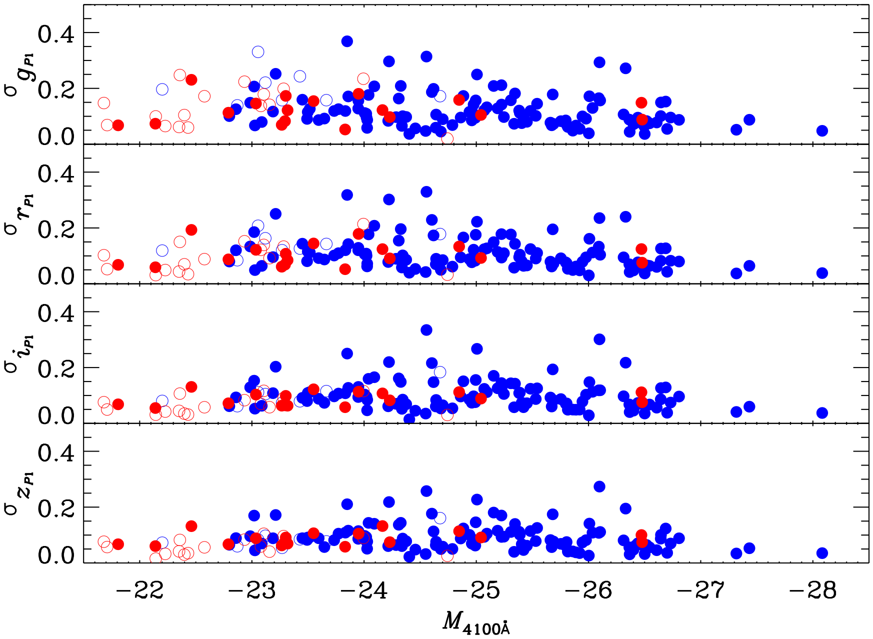

Figure 5. Distributions of the BVAs of the red and the typical QSOs as a function of the absolute magnitudes at 4100 Å, $M_{4100\ Å}$, in g_{P1}, r_{P1}, i_{P1}, and z_{P1} bands (from top to bottom), respectively. The red symbols represent the red QSOs, while the blue symbols represent the typical QSOs. The filled circles represent the SDSS-identified point sources, while the open circles represent the SDSS-identified extended sources.

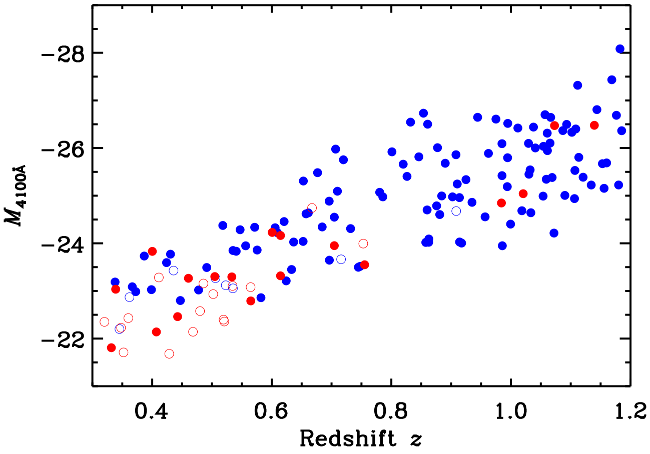

Figure 6. Absolute magnitudes of the selected QSOs at 4100 Å, $M_{4100\ Å}$, as a function of redshifts. The red symbols represent the red QSOs, while the blue symbols represent the typical QSOs. The filled circles represent the SDSS-identified point sources, while the open circles represent the SDSS-identified extended sources.

color of SDSS J233029.16+003746.5 is −0.739 from our spectral definition. Thus, it is also possible for this QSO to move out of the region of the typical QSO ($-0.785 < m_{3000\ Å} - m_{4000\ Å} < -0.565$). These results suggest that the color variabilities of some QSOs are capable of changing the color classification of these QSOs.

5.1. Host Galaxy Contamination

We found that 16 of 34 red QSOs and eight of 122 typical QSOs are identified as extended sources by SDSS, and most of these sources are located at low redshifts and are less luminous. Furthermore, most of the extended red QSOs exhibit evident decrease for both BVAs and CVAs with increasing wavelengths. A QSO is more variable than its host galaxy, thus the variation of a “QSO+host galaxy” system is originated from the variation of the QSO. Furthermore, A QSO is bluer than its host galaxy; therefore, the luminosity of a QSO is relatively more dominant at shorter wavelengths compared with its host galaxy, and the dominance may decrease at longer wavelengths. Since the QSO emission is the source of the variability and dominates at short wavelength, the variability amplitudes are expected to decrease with increasing wavelength. This is consistent with our results that the extended QSOs display

Table 2
Statistical Comparison of BVAs between the Typical and the Red QSOs

Filter	$\overline{\sigma}_{\rm typ}$	$\overline{\sigma}_{\rm red}$	p-value
	Brightness Variability (All QSOs)		
g_{P1}	0.1245	0.1278	0.677
r_{P1}	0.1103	0.0993	0.893
i_{P1}	0.1017	0.0774	0.077
z_{P1}	0.0918	0.0734	0.260
	Brightness Variability (Point-like QSOs)		
g_{P1}	0.1191	0.1214	0.851
r_{P1}	0.1080	0.1038	0.962
i_{P1}	0.1017	0.0884	0.364
z_{P1}	0.0922	0.0872	0.349
	Brightness Variability (“Extended” QSOs)		
g_{P1}	0.2022	0.1350	0.093
r_{P1}	0.1428	0.0942	0.093
i_{P1}	0.1013	0.0650	0.041
z_{P1}	0.0863	0.0579	0.093

Note. Comparisons for all QSOs are presented from row 1 to row 4; the results for the point-like QSOs (rows 5–8) and the “extended” QSOs (rows 9–12) are also presented. $\overline{\sigma}_{\rm typ}$ and $\overline{\sigma}_{\rm red}$: arithmetic mean of the BVAS for the typical and the red QSOs. p-value: p-value of the K–S static, referring to the probability of the occurrence of the observed BVAS, under the null hypothesis that the distributions of BVAS for the typical and the red QSOs are the same.

Table 3
Statistical Comparison of CVAs between the Typical and the Red QSOs

Color	$\overline{\sigma}_{\mathrm{typ}}$	$\overline{\sigma}_{\mathrm{red}}$	p-value
All QSOs			
$g_{P1} - r_{P1}$	0.0253	0.0403	3.51×10^{-4}
$r_{P1} - i_{P1}$	0.0231	0.0379	1.82×10^{-5}
$i_{P1} - z_{P1}$	0.0243	0.0286	0.033
$z < 0.6$			
$g_{P1} - r_{P1}$	0.0386	0.0484	0.245
$r_{P1} - i_{P1}$	0.0408	0.0385	0.418
$i_{P1} - z_{P1}$	0.0368	0.0274	0.251
$M_{4100\,\text{Å}} > -24$			
$g_{P1} - r_{P1}$	0.0371	0.0449	0.335
$r_{P1} - i_{P1}$	0.0422	0.0417	0.755
$i_{P1} - z_{P1}$	0.0389	0.0291	0.342
"Extended" QSOs			
$g_{P1} - r_{P1}$	0.0643	0.0516	0.838
$r_{P1} - i_{P1}$	0.0517	0.0411	0.354
$i_{P1} - z_{P1}$	0.0285	0.0181	0.354
Point-like QSOs			
$g_{P1} - r_{P1}$	0.0225	0.0302	7.34×10^{-3}
$r_{P1} - i_{P1}$	0.0211	0.0350	1.38×10^{-4}
$i_{P1} - z_{P1}$	0.0239	0.0379	2.31×10^{-4}
Point-like QSOs ($z < 0.6$)			
$g_{P1} - r_{P1}$	0.0262	0.0320	0.433
$r_{P1} - i_{P1}$	0.0359	0.0375	0.134
$i_{P1} - z_{P1}$	0.0403	0.0402	0.253
Point-like QSOs ($M_{4100\,\text{Å}} > -24$)			
$g_{P1} - r_{P1}$	0.0267	0.0323	0.386
$r_{P1} - i_{P1}$	0.0384	0.0404	0.167
$i_{P1} - z_{P1}$	0.0424	0.0424	0.660

Note. Comparison for all QSOs are presented from rows 1–3; results for the low-redshift QSOs (rows 4–6), less luminous QSOs (rows 7–9), extended QSOs (rows 10–12), point-like QSOs (rows 13–15), low-redshift point-like QSOs (rows 16–18) and less luminous point-like QSOs (rows 19–21) are also presented. $\overline{\sigma}_{\mathrm{typ}}$ and $\overline{\sigma}_{\mathrm{red}}$: arithmetic mean of variability amplitudes for the typical and the red QSOs. p-value: p-value of the K–S static, referring to the probability of the occurrence of the observed variability amplitudes, under the null hypothesis that the distributions of variability amplitudes for the typical and the red QSOs are the same.

evident decrease for both BVAs and CVAs with increasing wavelengths. In addition, the results also imply that the color variabilities of these extended QSOs might be directly originated from the internal brightness variabilities of the QSO; thus it is possible for these QSOs to generate the rapid color variabilities that we observed since the brightness of the QSOs vary rapidly.

Most QSOs show a bluer-when-brighter (BWB) trend. We fitted the g_{P1} and r_{P1} band light curves with the $g_{P1} - r_{P1}$ color light curve for an individual QSO to derive the color–magnitude slope of the QSO. A positive color–magnitude slope suggests a BWB trend; the greater the slope, the stronger the trend. The distributions of the slopes are shown in Figure 10. We find that most of our QSOs exhibit a BWB trend (positive slope). Figure 10 also show that the extended QSOs exhibit much greater slopes than the point-like QSOs, indicating that the extended QSOs have stronger BWB tendency. Because the host galaxy is redder than the blue QSO, when the QSO becomes brighter, the whole system becomes bluer. In other words, a BWB trend would be a natural consequence of the host galaxy contamination. Our results are consistent with that the extended QSOs are relatively faint QSOs with red host galaxies; such systems may exhibit a stronger BWB trend caused by the galaxy contamination.

5.2. Dust Reddening

We also studied how dust reddening might affect the spectra of QSOs. We applied the extinction curve of the Small Magellanic Cloud (SMC) (Pei 1992) on a typical QSO template to generate dust-reddened spectra with different extinction levels. From our results, some red QSO spectra can be well explained as dust-reddened spectra of typical QSOs; for example, the spectrum of SDSS J232710.78+001703.7, a red QSO with extended morphology, can be well matched as a dust-reddened spectrum of a typical QSO with $A_B = 1$ (left panel of Figure 11). We note that the CVA of SDSS J232710.78+001703.7 is weak, and the CVAs increase with increasing wavelengths, i.e., the CVA is 0.009 in $g_{P1} - r_{P1}$, 0.014 in $r_{P1} - i_{P1}$, and 0.022 in $i_{P1} - z_{P1}$. These results suggest that the reddening of the red QSO SDSS J232710.78+001703.7 is mainly caused by dust extinction of its host galaxy. However, some other point-like red QSOs with great CVAs, e.g., SDSS J221317.02+003714.1 (with CVAs equal to 0.033, 0.077 and 0.068 in $g_{P1}{-}r_{P1}$, $r_{P1}{-}i_{P1}$ and $i_{P1}{-}z_{P1}$) and SDSS J095823.73+011235.7 (with CVAs equal to 0.068, 0.049 and 0.056 in $g_{P1}{-}r_{P1}$, $r_{P1}{-}i_{P1}$ and $i_{P1}{-}z_{P1}$), also have spectra that can be approximately fitted with a dust-reddening spectrum of a typical QSO (Figure 12). We note that the color variabilities of the point-like red QSO SDSS J095823.73+011235.7 are capable of changing color significantly to become much redder or bluer as discussed earlier. If dust reddening is causing the spectral changes, the size scale on which the dust-reddening material is located must be of order of a few light years. If the color variability is not due to changing dust obscuration, other physical mechanisms must account for the red spectrum. On the other hand, most of the red QSO spectra are difficult to explain in terms of dust extinction, such as SDSS J232545.18−004309.1 (right panel of Figure 11). The spectrum of SDSS J232545.18−004309.1 exhibits a "bump structure" from 3000 to 4000 Å, which is difficult to explain in terms of dust reddening of a typical QSO spectrum. Some QSO spectra display a "small blue bump" around 2200–4000 Å, which is mainly caused by multiple blended Fe II emission and the Balmer recombination continuum (Wills et al. 1985).

5.3. Influence of Emission Lines

The color variabilities might be influenced by strong emission lines. At different redshifts, some strong emission lines might be redshifted into the spectral regions of the photometric filters that we used to investigate the color variabilities of QSOs. To investigate the influence of strong emission lines, we consider the affects of the following emission lines: [N III] (1908 Å), [Mg II] (2799 Å), [O II] (3725 Å), [O II] (3727 Å), H δ (4102 Å), H γ (4342 Å), H β (4861 Å), [O III] (4960 Å), [O III] (5008 Å), and H α (6563 Å).

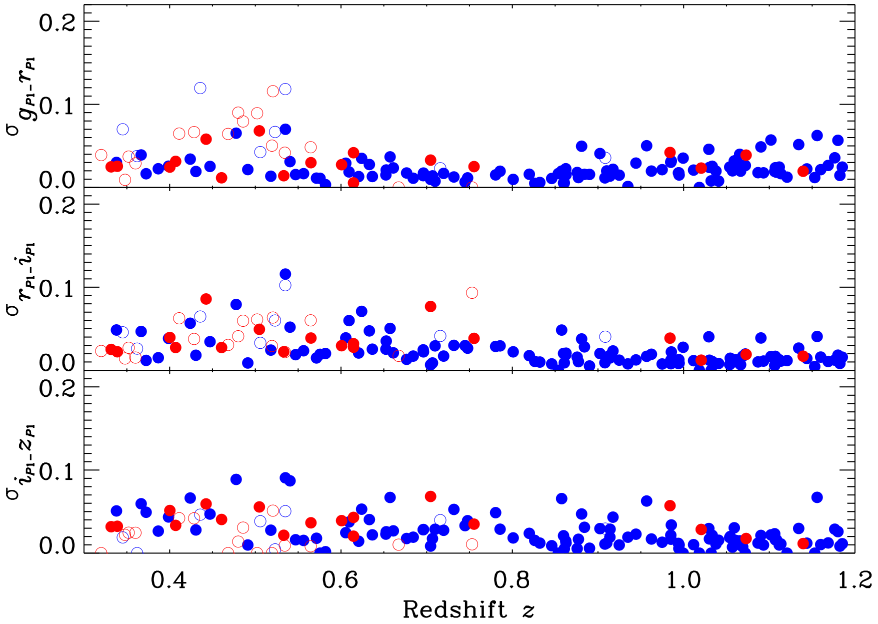

Figure 7. Distributions of the CVAs of the red and the typical QSOs as a function of redshift in g_{P1}−r_{P1}, r_{P1}−i_{P1}, and i_{P1}−z_{P1} color (from top to bottom), respectively. The red symbols represent the red QSOs, while the blue symbols represent the typical QSOs. The filled circles represent the SDSS-identified point sources, while the open circles represent the SDSS-identified extended sources.

We estimated the mean CVAs separately for both emission-line-affected (ELA) and non-emission-line-affected (NELA) QSOs. We find the mean CVAs of the whole QSO sample are similar to those of the ELA QSOs and the NELA QSOs (Table 5); the K–S test p-values of the corresponding CVAs are also shown in Table 5, indicating that the distributions of the CVAs between the whole QSO samples, the ELA QSOs, and the NELA QSOs are indistinguishable. These results suggest that the emission lines do not affect our results.

5.4. Influence of Cosmological Time Dilation

We have observed that QSOs at high redshifts have lower CVAs. However, owing to cosmological time dilation, the variabilities of the QSOs occurring at high redshifts were actually measured in shorter time intervals in their rest frame than those at low redshifts. To account for the influence of different timeframes in the variability results, we adopted another method to quantify CVAs over different time intervals:

$$\sigma = \frac{1}{n-1}\sum_{i=1}^{n-1}\frac{|C_{n+1}-C_n|}{(t_{n+1}-t_n)/(z+1)}, \qquad (7)$$

where z represents the redshift; C_{n+1}−C_n represents the color difference between the nth and the $(n+1)$th observations, and t_{n+1}−t_n represents the time separation between the nth and the $(n+1)$th observations.

If we neglect the cosmological time dilation, the K–S test p-values of the CVAs defined above between the typical and the red QSOs are 9.42×10^{-8}, 1.26×10^{-6}, and 5.03×10^{-6} in g_{P1}−r_{P1}, r_{P1}−i_{P1}, and i_{P1}−z_{P1}, respectively; if the cosmological time dilation is taken into account, the p-values become 3.04×10^{-5}, 9.78×10^{-6}, and 5.69×10^{-4} in g_{P1}−r_{P1}, r_{P1}−i_{P1}, and i_{P1}−z_{P1}. The results suggest that the difference of the CVA distributions between the red and the typical QSOs are not due to cosmological time dilation. Furthermore, the K–S test p-values of the CVAs between the point-like red and the point-like typical QSOs are 0.009, 0.003 and 0.004 in g_{P1}−r_{P1}, r_{P1}−i_{P1}, and i_{P1}−z_{P1} if the cosmological time dilation is neglected. The p-values become 0.014, 0.052 and 0.043 if we take into account the cosmological time dilation. The distributions of the CVAs between the point-like typical and the point-like red QSOs are different, even with the consideration of the cosmological time dilation. These results suggest that the cosmological time dilation does not affect our results.

6. Summary

We selected a group of red QSOs and a group of typical QSOs at $z = 0.3$–1.2 based on the ratios of their spectral flux densities at 3000 Å to those at 4000 Å in the rest frame (see Table 6 and Table 7 for the red QSOs and the typical QSOs, respectively). We studied the brightness and color variabilities of 34 red QSOs and 122 typical QSOs (see Table 8 and Table 9) using data from the MDS of the Panoramic Survey Telescope and Rapid Response System (PS1). We find that most of the red QSOs we obtained are relatively less luminous and occur at low redshift; however, there are four luminous red QSOs that are as bright as typical QSOs and are observed at high redshifts. We note that there are 16 of 34 red QSOs and eight of 122 typical QSOs are extended sources identified by SDSS. The redshifts of the selected QSOs are well related to their luminosities; the relation is caused by the Malmquist bias.

We estimated the BVAs and the CVAs for the red and the typical QSOs. The distributions of BVAs between the red and the typical QSOs are similar. The majority of the low-redshift red QSOs are extended sources, which makes these red QSOs more variable at shorter wavelengths than at longer wavelengths because of the contamination of the emission from the host galaxies. The point-like red QSOs are more color variable than the point-like typical QSOs; nevertheless, at low redshifts ($z < 0.6$), the CVA difference is not significant between the point-like red QSOs and the point-like typical ones.

The CVAs of the red and the typical QSOs are not due to strong emission lines and cosmological time dilation. We find that several point-like QSOs exhibit significant CVAs;

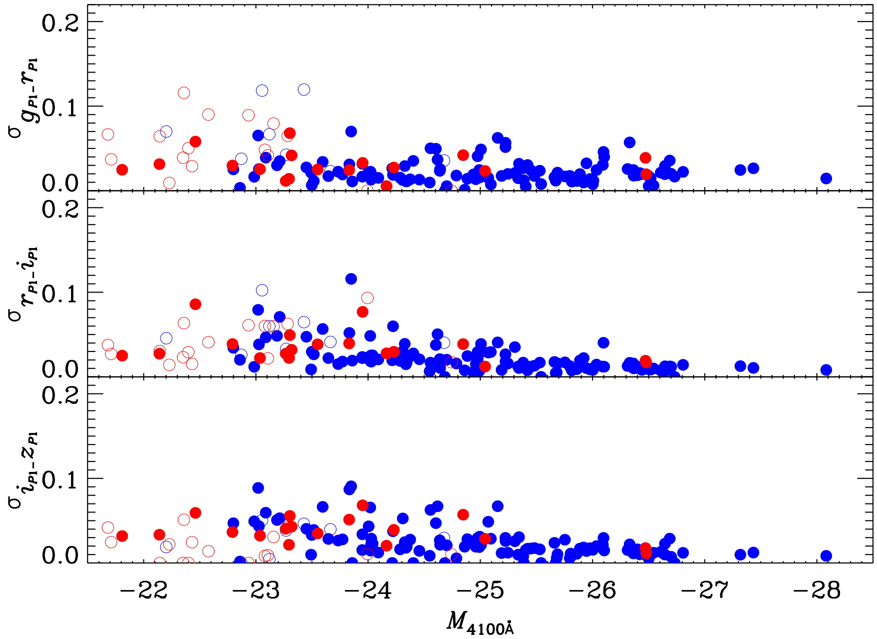

Figure 8. Distributions of the CVAs of the red and the typical QSOs as a function of $M_{4100\,\text{Å}}$ in $g_{P1}-r_{P1}$, $r_{P1}-i_{P1}$, and $i_{P1}-z_{P1}$ color (from top to bottom), respectively. The red symbols represent the red QSOs, while the blue symbols represent the typical QSOs. The filled circles represent the SDSS-identified point sources, while the open circles represent the SDSS-identified extended sources.

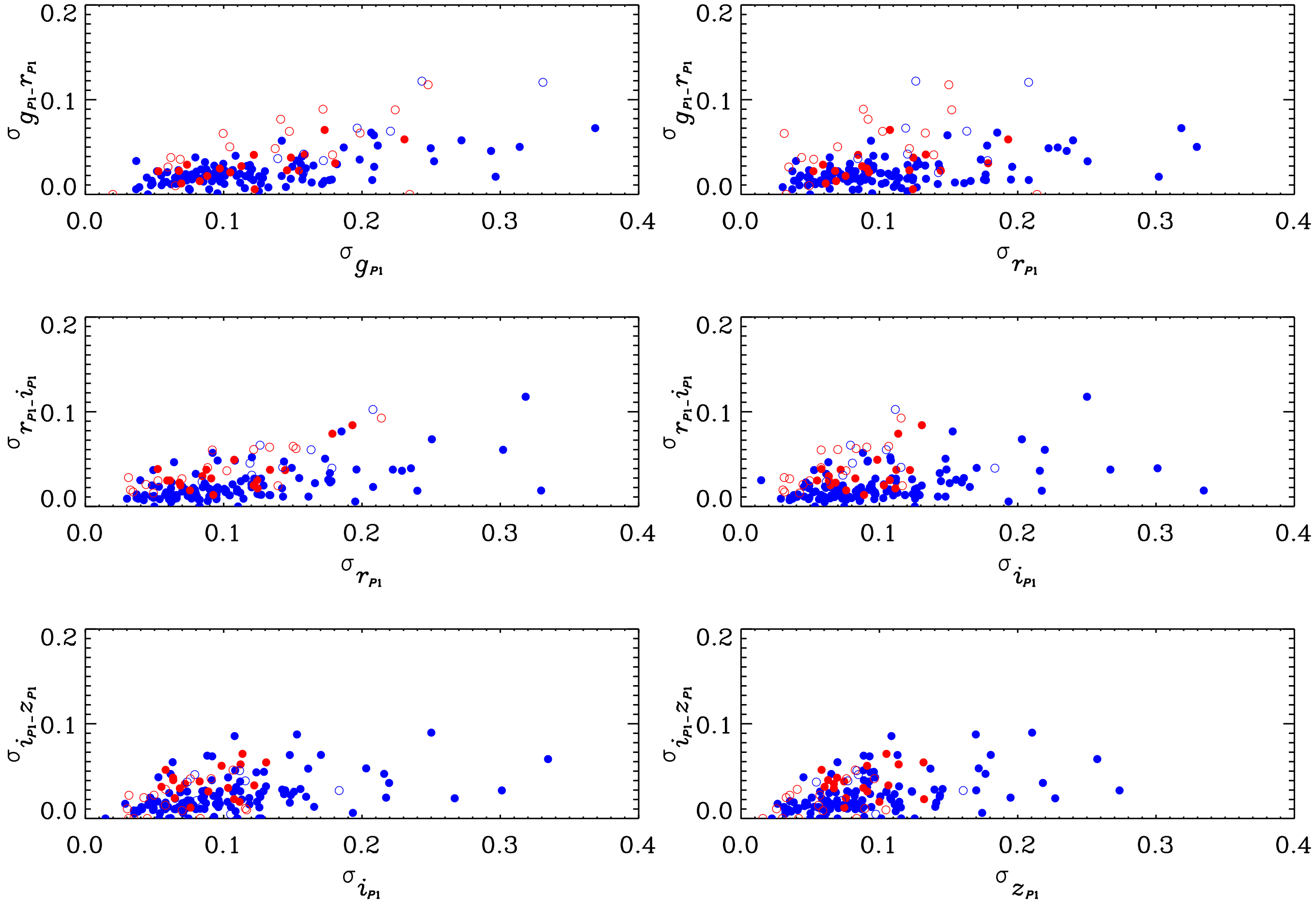

Figure 9. Correlations between the BVAs and the CVAs. Top left: σ_{gP1} vs. $\sigma_{gP1-rP1}$; top right: σ_{rP1} vs. $\sigma_{rP1-iP1}$; middle left: σ_{rP1} vs. $\sigma_{rP1-iP1}$; middle right: σ_{iP1} vs. $\sigma_{iP1-zP1}$; bottom left: σ_{iP1} vs. $\sigma_{iP1-zP1}$; and bottom right: σ_{zP1} vs. $\sigma_{iP1-zP1}$. The red symbols represent the red QSOs, while the blue symbols represent the typical QSOs. The filled circles represent the SDSS-identified point sources, while the open circles represent the SDSS-identified extended sources.

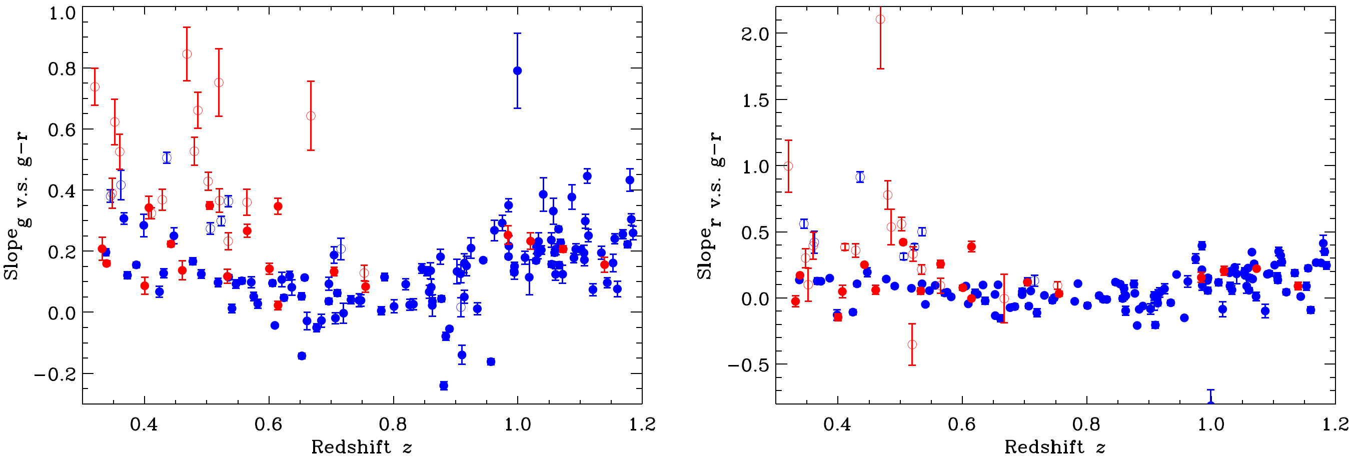

Figure 10. Distributions of the slopes in $(g_{P1}-r_{P1})-g_{P1}$ (left panel) and $(g_{P1}-r_{P1})-r_{P1}$ (right panel) color–magnitude plane as a function of redshift. Positive slope indicates a bluer-when-brighter (BWB) trend. The red symbols represent the red QSOs, while the blue symbols represent the typical QSOs. The filled circles represent the SDSS-identified point sources, while the open circles represent the SDSS-identified extended sources.

Table 4
Correlation between the Observed BVAs and CVAs

	Typical QSO		Red QSO	
	r	*p*-value	*r*	*p*-value
All QSOs				
$\sigma_{g_{P1}}$ versus $\sigma_{g_{P1}-r_{P1}}$	0.653	4.44×10^{-16}	0.579	3.29×10^{-4}
$\sigma_{r_{P1}}$ versus $\sigma_{g_{P1}-r_{P1}}$	0.450	2.29×10^{-7}	0.218	0.216
$\sigma_{r_{P1}}$ versus $\sigma_{r_{P1}-i_{P1}}$	0.577	4.17×10^{-12}	0.758	2.03×10^{-7}
$\sigma_{i_{P1}}$ versus $\sigma_{r_{P1}-i_{P1}}$	0.395	7.20×10^{-6}	0.478	0.004
$\sigma_{i_{P1}}$ versus $\sigma_{i_{P1}-z_{P1}}$	0.447	2.74×10^{-7}	0.442	0.009
$\sigma_{z_{P1}}$ versus $\sigma_{i_{P1}-z_{P1}}$	0.440	4.29×10^{-7}	0.469	0.005
Point-like QSOs				
$\sigma_{g_{P1}}$ versus $\sigma_{g_{P1}-r_{P1}}$	0.604	1.43×10^{-12}	0.667	0.003
$\sigma_{r_{P1}}$ versus $\sigma_{g_{P1}-r_{P1}}$	0.510	7.92×10^{-9}	0.428	0.076
$\sigma_{r_{P1}}$ versus $\sigma_{r_{P1}-i_{P1}}$	0.572	3.73×10^{-11}	0.701	0.001
$\sigma_{i_{P1}}$ versus $\sigma_{r_{P1}-i_{P1}}$	0.457	3.61×10^{-7}	0.492	0.038
$\sigma_{i_{P1}}$ versus $\sigma_{i_{P1}-z_{P1}}$	0.459	3.07×10^{-7}	0.266	0.286
$\sigma_{z_{P1}}$ versus $\sigma_{i_{P1}-z_{P1}}$	0.461	2.76×10^{-7}	0.186	0.460

Note. *r*: pearson correlation coefficient between BVAs and CVAs; *p*-value: *p*-value of the two-sided t-test, referring to the probability of an uncorrelated system producing data sets that have a pearson correlation at least as extreme as the one computed from these data sets.

the color variabilities of these QSOs are capable of changing their color classification in our definition. The timescales of the color variability of these QSOs are quite short, on the order of years, suggesting that the size scales of the mechanism producing the color variability might be less than a few light years, e.g., red synchrotron emission (Benn et al. 1998; Whiting et al. 2001).

The spectra of some extended red QSOs can be well fitted as the dust-reddened spectra of a typical QSO, e.g., SDSS J232710.78+001703.7 (left panel of Figure 11). The CVAs of SDSS J232710.78+001703.7 are weak and do not increase with increasing wavelengths. These results suggest that the redness of this red QSO is caused by dust reddening, which is likely originated from the host galaxy of this QSO. On the other hand, some point-like red QSOs with strong color variabilities also show dust-reddening spectra, e.g., SDSS J095823.73+011235.7 (left panel of Figure 12). If the color variabilities of these red QSOs are caused by dust reddening, the reddening material should be on scales smaller than a few light years, If the color variabilities are not due to changing dust obscuration, other physical mechanisms must account for the red spectrum. Furthermore, the spectra of some point-like red QSOs

Table 5

Statistical Comparison between the Emission-lines-affected (ELA) QSOs and the Non-emission-lines-affected (NELA) QSOs

Color	$\overline{\sigma}_{\rm typ}$	$\overline{\sigma}_{\rm red}$
ELA QSOs		
$g_{P1}-r_{P1}$	0.0244	0.0431
$r_{P1}-i_{P1}$	0.0223	0.0320
$i_{P1}-z_{P1}$	0.0216	0.0350
NELA QSOs		
$g_{P1}-r_{P1}$	0.0259	0.0371
$r_{P1}-i_{P1}$	0.0240	0.0430
$i_{P1}-z_{P1}$	0.0272	0.0263
	K–S Test between All, ELA, and NELA QSOs	
Color		p-value
ELA Typical QSOs versus All Typical QSOs		
$g_{P1}-r_{P1}$		0.999
$r_{P1}-i_{P1}$		0.998
$i_{P1}-z_{P1}$		0.974
ELA Red QSOs versus All Red QSOs		
$g_{P1}-r_{P1}$		0.923
$r_{P1}-i_{P1}$		0.967
$i_{P1}-z_{P1}$		0.676
NELA Typical QSOs versus All Typical QSOs		
$g_{P1}-r_{P1}$		0.999
$r_{P1}-i_{P1}$		0.999
$i_{P1}-z_{P1}$		0.933
NELA Red QSOs versus All Red QSOs		
$g_{P1}-r_{P1}$		0.869
$r_{P1}-i_{P1}$		0.985
$i_{P1}-z_{P1}$		0.999
ELA Typical QSOs versus NELA Typical QSOs		
$g_{P1}-r_{P1}$		0.891
$r_{P1}-i_{P1}$		0.962
$i_{P1}-z_{P1}$		0.408
ELA Red QSOs versus NELA Red QSOs		
$g_{P1}-r_{P1}$		0.268
$r_{P1}-i_{P1}$		0.495
$i_{P1}-z_{P1}$		0.330

Note. $\overline{\sigma}_{\rm typ}$, $\overline{\sigma}_{\rm red}$ and p-value: similar to the description in Tables 2 and 3.

are difficult to explain in terms of the dust extinction, e.g., SDSS J232545.18−004309.1 (right panel of Figure 11); this QSO also exhibit strong color variabilities. These results imply that the reddening mechanism should come from the QSO itself.

In summary, we find that the colors of some QSOs can vary significantly with timescales of a few years. The color variations may also change the color classification of the QSOs. The rapid color variations could be due to small size scale dust reddening, or other rapid physical mechanisms. Our results suggest that there are different types of red QSOs with different origins, which require further investigation.

This work was partially supported by the Ministry of Science and Technology (MOST) of Taiwan through grant MOST 106-2119-M-008-016.

The PS1 Surveys have been made possible under the contributions of the Institute for Astronomy, the University of Hawaii, the Pan-STARRS Project Office, the Max Planck Society and its participating institutes, the Max Planck Institute

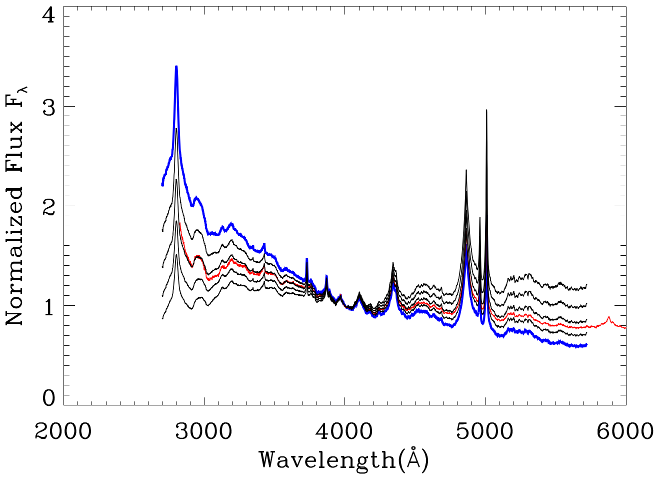

Figure 11. Dust-reddening effect on a typical QSO spectrum. The rest-frame spectra of two red QSOs: SDSS J232710.78+001703.7 (left panel) and SDSS J232545.18−004309.1 (right panel), normalized at 4000 Å, are shown as the red lines. The blue line shows a composite spectrum of all typical QSOs in the redshift range $0.4 < z < 0.5$. The four black lines are reddened versions of the composite spectrum, generated with the extinction curves of Small Magellanic Cloud (SMC) mentioned in Pei (1992), with A_B equal to 0.5, 1, 1.5, and 2.

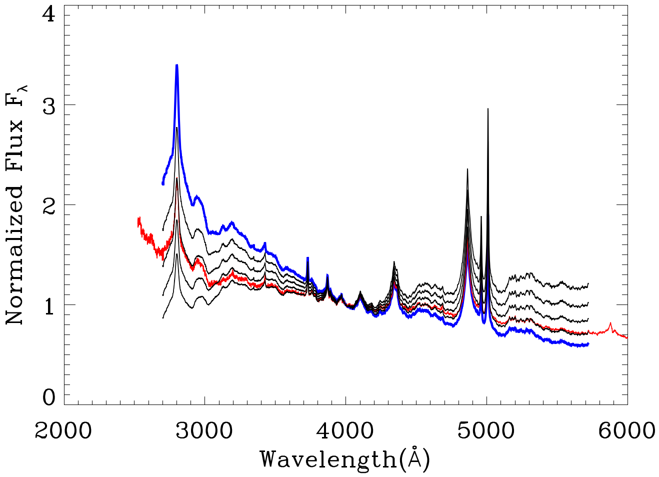

Figure 12. Dust-reddening effect on a typical QSO spectrum. The rest-frame spectra of two red QSOs: SDSS J095823.73+011235.7 (left panel) and SDSS J221317.02+003714.1 (right panel), normalized at 4000 Å, are shown as the red lines. The blue line shows a composite spectrum of all typical QSOs in the redshift range $0.4 < z < 0.5$. The four black lines are reddened versions of the composite spectrum, generated with the extinction curves of Small Magellanic Cloud (SMC) mentioned in Pei (1992), with A_B equal to 0.5, 1, 1.5, and 2.

for Astronomy, Heidelberg and the Max Planck Institute for Extraterrestrial Physics, Garching, The Johns Hopkins University, Durham University, the University of Edinburgh, Queens University Belfast, the Harvard-Smithsonian Center for Astrophysics, the Las Cumbres Observatory Global Telescope Network Incorporated, the National Central University of Taiwan, the Space Telescope Science Institute, the National Aeronautics and Space Administration under grant No. NNX08AR22G issued through the Planetary Science Division of the NASA Science Mission Directorate, the National Science Foundation under grant No. AST-1238877, and the University of Maryland.

Appendix A
Information of the Selected QSOs

We present the basic information for the red QSOs and the typical QSOs in Table 6 and Table 7, respectively.

Table 6
Information of the Red QSOs

Name	R.A.(J2000)	Decl.(J2000)	MD Field	Redshift	$M_{4100\ \text{Å}}$	Obj. Type
SDSS J083732.19+450139.7	129.3840	45.0277	MD03	1.140	−26.478	STAR
SDSS J095823.73+011235.7	149.5990	1.2099	MD04	0.505	−23.302	STAR
SDSS J095915.20+031617.4	149.8130	3.2715	MD04	0.461	−23.266	STAR
SDSS J100027.43+025951.3	150.1140	2.9976	MD04	0.339	−23.036	STAR
SDSS J100043.13+020637.2	150.1800	2.1103	MD04	0.360	−22.431	GALAXY
SDSS J221110.98−000953.3	332.7960	−0.1648	MD09	0.667	−24.743	GALAXY
SDSS J221155.73−001043.9	332.9820	−0.1789	MD09	0.400	−23.831	STAR
SDSS J221317.02+003714.1	333.3210	0.6206	MD09	0.705	−23.951	STAR
SDSS J221337.66−002017.5	333.4070	−0.3382	MD09	1.073	−26.472	STAR
SDSS J221348.77−005007.8	333.4530	−0.8355	MD09	0.984	−24.847	STAR
SDSS J221356.01−002455.7	333.4830	−0.4155	MD09	1.020	−25.042	STAR
SDSS J221412.45−001009.7	333.5520	−0.1694	MD09	0.352	−21.710	GALAXY
SDSS J221424.68−005221.7	333.6030	−0.8727	MD09	0.521	−22.358	GALAXY
SDSS J221449.38+011525.3	333.7060	1.2571	MD09	0.486	−23.157	GALAXY
SDSS J221512.15−005152.5	333.8010	−0.8646	MD09	0.519	−22.398	GALAXY
SDSS J221707.16−004721.9	334.2800	−0.7894	MD09	0.755	−23.550	STAR
SDSS J221712.61−002502.8	334.3030	−0.4175	MD09	0.442	−22.461	STAR
SDSS J221715.18+002615.0	334.3130	0.4375	MD09	0.753	−23.994	GALAXY
SDSS J221715.70+005630.2	334.3150	0.9417	MD09	0.320	−22.351	GALAXY
SDSS J221750.50−002425.9	334.4600	−0.4072	MD09	0.601	−24.229	STAR
SDSS J221826.14+000012.8	334.6090	0.0036	MD09	0.428	−21.681	GALAXY
SDSS J221907.95+004023.3	334.7830	0.6732	MD09	0.615	−23.318	STAR
SDSS J221917.01−000757.5	334.8210	−0.1327	MD09	0.407	−22.140	STAR
SDSS J221932.17−004551.9	334.8840	−0.7644	MD09	0.332	−21.808	STAR
SDSS J221956.75+005913.3	334.9860	0.9870	MD09	0.468	−22.143	GALAXY
SDSS J222000.58+010742.1	335.0020	1.1284	MD09	0.480	−22.577	GALAXY
SDSS J222133.75+010119.2	335.3910	1.0220	MD09	0.534	−23.106	GALAXY
SDSS J232458.66−000302.9	351.2440	−0.0508	MD10	0.533	−23.295	STAR
SDSS J232545.18−004309.1	351.4380	−0.7192	MD10	0.565	−23.080	GALAXY
SDSS J232710.78+001703.7	351.7950	0.2844	MD10	0.348	−22.228	GALAXY
SDSS J232712.98−003618.3	351.8040	−0.6051	MD10	0.565	−22.791	STAR
SDSS J232801.47+001705.0	352.0060	0.2847	MD10	0.411	−23.283	GALAXY
SDSS J232953.52+005106.6	352.4730	0.8518	MD10	0.502	−22.934	GALAXY
SDSS J233129.83−004933.2	352.8740	−0.8259	MD10	0.615	−24.164	STAR

Note. Name: object name; R.A.: right ascension; decl.: declination; MD field: MD field that the QSO belongs to, redshift: spectral redshift of the QSO, $M_{4100\ \text{Å}}$: absolute magnitudes defined with the spectral region around 4100 Å. and Obj. Type: object type parameter in the SDSS DR7 quasar catalog; "GALAXY" represent for extended source while "STAR" represent for point source.

Table 7
Same as Table 6, but for the Typical QSOs

Name	R.A.(J2000)	Decl.(J2000)	MD Field	Redshift	$M_{4100\,\text{Å}}$	Obj. Type
SDSS J083924.96+442106.0	129.8540	44.3517	MD03	0.995	−26.518	STAR
SDSS J083950.19+432941.3	129.9590	43.4948	MD03	0.556	−23.948	STAR
SDSS J084101.70+425806.4	130.2570	42.9685	MD03	0.890	−25.681	STAR
SDSS J084140.62+434908.5	130.4190	43.8190	MD03	1.169	−27.434	STAR
SDSS J084146.01+450443.4	130.4420	45.0787	MD03	1.059	−25.345	STAR
SDSS J084153.02+443157.0	130.4710	44.5325	MD03	0.696	−24.885	STAR
SDSS J084221.84+453516.2	130.5910	45.5878	MD03	0.745	−23.498	STAR
SDSS J084512.98+445209.0	131.3040	44.8692	MD03	1.030	−25.451	STAR
SDSS J095530.55+021652.8	148.8770	2.2814	MD04	0.748	−23.516	STAR
SDSS J095642.33+020554.4	149.1760	2.0985	MD04	1.032	−25.542	STAR
SDSS J095656.19+021315.1	149.2340	2.2209	MD04	1.121	−25.388	STAR
SDSS J095705.13+014949.5	149.2710	1.8304	MD04	1.134	−25.224	STAR
SDSS J095819.87+022903.4	149.5830	2.4843	MD04	0.345	−22.201	GALAXY
SDSS J095945.61+013032.1	149.9400	1.5090	MD04	1.106	−24.939	STAR
SDSS J095946.01+024743.5	149.9420	2.7954	MD04	1.065	−26.104	STAR
SDSS J100025.24+015852.0	150.1050	1.9811	MD04	0.373	−22.985	STAR
SDSS J100104.86+011421.2	150.2700	1.2392	MD04	1.018	−24.684	STAR
SDSS J100106.38+030309.8	150.2770	3.0527	MD04	0.609	−24.222	STAR
SDSS J100119.69+010501.7	150.3320	1.0838	MD04	1.108	−26.401	STAR
SDSS J100125.46+005205.5	150.3560	0.8682	MD04	0.780	−25.071	STAR
SDSS J100210.72+023026.1	150.5450	2.5073	MD04	1.160	−25.688	STAR
SDSS J100226.98+033039.7	150.6120	3.5110	MD04	0.910	−25.246	STAR
SDSS J100229.01+010858.4	150.6210	1.1496	MD04	0.684	−24.344	STAR
SDSS J100232.13+023537.3	150.6340	2.5937	MD04	0.657	−24.619	STAR
SDSS J100324.56+021831.3	150.8520	2.3087	MD04	0.518	−24.375	STAR
SDSS J100327.67+015742.3	150.8650	1.9618	MD04	1.066	−26.644	STAR
SDSS J100333.99+024126.2	150.8920	2.6906	MD04	0.985	−25.421	STAR
SDSS J100421.01+013647.3	151.0880	1.6132	MD04	1.038	−26.440	STAR
SDSS J100429.00+025209.2	151.1210	2.8692	MD04	0.877	−26.008	STAR
SDSS J104239.65+583230.9	160.6650	58.5420	MD05	0.994	−25.797	STAR
SDSS J104405.38+570024.2	161.0220	57.0067	MD05	0.447	−22.799	STAR
SDSS J104556.84+570747.0	161.4870	57.1298	MD05	0.540	−23.833	STAR
SDSS J104625.02+584839.1	161.6040	58.8109	MD05	0.576	−23.859	STAR
SDSS J104633.70+571530.4	161.6400	57.2584	MD05	0.710	−25.094	STAR
SDSS J104659.37+573055.8	161.7470	57.5155	MD05	1.029	−26.098	STAR
SDSS J104757.52+573451.8	161.9900	57.5811	MD05	1.102	−26.331	STAR
SDSS J104859.67+565648.6	162.2490	56.9468	MD05	1.012	−26.421	STAR
SDSS J105000.21+581904.2	162.5010	58.3179	MD05	0.832	−26.544	STAR
SDSS J105141.16+591305.2	162.9220	59.2181	MD05	0.436	−23.428	GALAXY
SDSS J105239.60+572431.3	163.1650	57.4087	MD05	1.112	−27.318	STAR
SDSS J121440.10+473226.2	183.6670	47.5406	MD06	1.061	−26.313	STAR
SDSS J121729.40+471424.8	184.3730	47.2402	MD06	1.041	−26.003	STAR
SDSS J121934.41+465155.4	184.8930	46.8654	MD06	0.786	−24.976	STAR
SDSS J121946.40+473748.1	184.9430	47.6301	MD06	0.652	−24.040	STAR
SDSS J122025.31+480531.3	185.1050	48.0920	MD06	0.661	−24.639	STAR
SDSS J122046.61+464347.4	185.1940	46.7299	MD06	0.707	−25.978	STAR
SDSS J122107.54+462736.0	185.2810	46.4600	MD06	0.653	−25.308	STAR
SDSS J122302.22+482036.0	185.7590	48.3433	MD06	0.606	−24.327	STAR
SDSS J122419.76+481104.2	186.0820	48.1845	MD06	0.854	−26.732	STAR
SDSS J122517.84+461126.8	186.3240	46.1908	MD06	0.431	−23.772	STAR
SDSS J122607.92+473700.5	186.5330	47.6168	MD06	1.054	−26.036	STAR
SDSS J141154.12+520023.4	212.9760	52.0065	MD07	0.962	−25.888	STAR
SDSS J141226.48+525347.6	213.1100	52.8965	MD07	1.144	−26.807	STAR
SDSS J141318.96+543202.4	213.3290	54.5340	MD07	0.362	−22.870	GALAXY
SDSS J141352.98+523444.2	213.4710	52.5790	MD07	0.860	−24.701	STAR
SDSS J141500.38+520658.5	213.7520	52.1163	MD07	0.424	−23.595	STAR
SDSS J141533.89+520558.0	213.8910	52.0995	MD07	0.985	−26.092	STAR
SBS 1415+541	214.2490	53.9685	MD07	0.720	−25.754	STAR
SDSS J141856.19+535845.0	214.7340	53.9792	MD07	0.975	−26.608	STAR
SDSS J142008.28+521646.8	215.0340	52.2797	MD07	1.057	−26.701	STAR
SDSS J142052.43+525622.4	215.2180	52.9396	MD07	0.677	−25.483	STAR
SDSS J160523.10+545613.3	241.3460	54.9371	MD08	0.571	−24.337	STAR
SDSS J160630.60+542007.5	241.6280	54.3354	MD08	0.820	−25.661	STAR
SDSS J221115.06−000030.9	332.8130	−0.0086	MD09	0.478	−23.020	STAR

Table 7
(Continued)

Name	R.A.(J2000)	Decl.(J2000)	MD Field	Redshift	$M_{4100\,\text{Å}}$	Obj. Type
SDSS J221203.19+000239.0	333.0130	0.0442	MD09	1.180	−25.225	STAR
SDSS J221301.63+004342.7	333.2570	0.7285	MD09	1.061	−25.946	STAR
SDSS J221337.97−004305.9	333.4080	−0.7183	MD09	1.182	−28.083	STAR
SDSS J221407.38+000727.1	333.5310	0.1242	MD09	0.914	−24.028	STAR
SDSS J221447.74−002032.6	333.6990	−0.3424	MD09	1.093	−26.497	STAR
SDSS J221619.25−002430.4	334.0800	−0.4085	MD09	0.881	−24.604	STAR
SDSS J221708.83+002717.1	334.2870	0.4548	MD09	1.113	−25.805	STAR
SDSS J221756.92+010119.5	334.4870	1.0221	MD09	0.861	−26.501	STAR
SDSS J221901.87+000025.9	334.7580	0.0072	MD09	1.153	−25.672	STAR
SDSS J221912.12+003612.9	334.8010	0.6036	MD09	0.826	−25.405	STAR
SDSS J222029.54+004401.3	335.1230	0.7337	MD09	0.621	−24.457	STAR
SDSS J222036.80−002051.9	335.1530	−0.3478	MD09	1.090	−25.006	STAR
SDSS J222123.28−001824.1	335.3470	−0.3067	MD09	0.846	−25.816	STAR
SDSS J222147.92−002205.8	335.4500	−0.3683	MD09	1.107	−25.530	STAR
SDSS J232355.04−001507.3	350.9790	−0.2521	MD10	0.399	−23.027	STAR
SDSS J232423.68−002320.6	351.0990	−0.3891	MD10	1.072	−24.215	STAR
SDSS J232428.36−005244.3	351.1180	−0.8790	MD10	0.506	−23.269	GALAXY
SDSS J232500.55−011445.0	351.2520	−1.2459	MD10	0.935	−24.861	STAR
SDSS J232515.93+002229.1	351.3160	0.3748	MD10	1.087	−26.367	STAR
SDSS J232525.32+000352.1	351.3560	0.0645	MD10	0.338	−23.188	STAR
SDSS J232525.52+001136.8	351.3560	0.1936	MD10	0.491	−23.492	STAR
SDSS J232554.37−001823.8	351.4770	−0.3066	MD10	0.999	−24.403	STAR
SDSS J232555.33+004109.9	351.4810	0.6861	MD10	1.176	−26.688	STAR
SDSS J232626.14+000922.2	351.6090	0.1562	MD10	1.033	−24.642	STAR
SDSS J232705.65−000648.5	351.7740	−0.1135	MD10	0.957	−24.556	STAR
SDSS J232712.41−001815.7	351.8020	−0.3044	MD10	0.944	−26.646	STAR
SDSS J232728.26+005341.4	351.8680	0.8949	MD10	1.185	−26.364	STAR
SDSS J232742.67+000653.9	351.9280	0.1150	MD10	0.884	−24.995	STAR
SDSS J232743.72+002837.0	351.9320	0.4769	MD10	0.523	−23.120	GALAXY
SDSS J232757.24−000035.9	351.9880	−0.0100	MD10	0.986	−23.949	STAR
SDSS J232757.95−002058.8	351.9910	−0.3497	MD10	1.069	−25.382	STAR
SDSS J232803.53−001656.3	352.0150	−0.2823	MD10	0.633	−23.450	STAR
SDSS J232825.86+004439.7	352.1080	0.7444	MD10	0.925	−25.337	STAR
SDSS J232833.50−005234.2	352.1400	−0.8762	MD10	0.858	−24.019	STAR
SDSS J232928.88−011405.6	352.3700	−1.2349	MD10	0.535	−23.055	GALAXY
SDSS J232930.16−000752.7	352.3760	−0.1313	MD10	0.862	−24.022	STAR
SDSS J233007.17−000324.4	352.5300	−0.0568	MD10	0.914	−24.960	STAR
SDSS J233010.93−002951.5	352.5460	−0.4976	MD10	0.547	−24.285	STAR
SDSS J233011.42−001800.1	352.5480	−0.3000	MD10	0.908	−25.860	STAR
SDSS J233020.71+001727.5	352.5860	0.2910	MD10	0.705	−24.549	STAR
SDSS J233023.48+000811.8	352.5980	0.1366	MD10	0.994	−25.190	STAR
SDSS J233027.81−005905.7	352.6160	−0.9849	MD10	1.054	−24.991	STAR
SDSS J233029.16+003746.5	352.6220	0.6296	MD10	0.535	−23.849	STAR
SDSS J233119.80−010632.3	352.8330	−1.1090	MD10	0.387	−23.733	STAR
SDSS J233133.07−005609.1	352.8880	−0.9359	MD10	0.637	−24.027	STAR
SDSS J233138.97−002429.2	352.9120	−0.4081	MD10	0.732	−24.309	STAR
SDSS J233139.32−001516.7	352.9140	−0.2547	MD10	0.801	−25.921	STAR
SDSS J233149.48+000719.4	352.9560	0.1221	MD10	0.367	−23.088	STAR
SDSS J233155.01−011515.0	352.9790	−1.2542	MD10	0.876	−24.787	STAR
SDSS J233157.77−005130.9	352.9910	−0.8586	MD10	0.582	−22.858	STAR
SDSS J233229.37+002740.3	353.1220	0.4612	MD10	0.624	−23.212	STAR
SDSS J233230.41+000137.6	353.1270	0.0271	MD10	0.716	−23.664	GALAXY
SDSS J233315.84−000452.8	353.3160	−0.0813	MD10	0.696	−23.646	STAR
SDSS J233325.16−005835.2	353.3550	−0.9765	MD10	1.156	−25.155	STAR
SDSS J233329.00−000308.1	353.3710	−0.0523	MD10	0.918	−24.005	STAR
SDSS J233330.57−004832.2	353.3770	−0.8090	MD10	0.863	−24.091	STAR
SDSS J233409.36−010118.0	353.5390	−1.0216	MD10	0.909	−24.677	GALAXY
SDSS J233411.74−011131.1	353.5490	−1.1920	MD10	0.902	−24.976	STAR

Appendix B
Results of Variability

We present the results of BVAs and CVAs for the red QSOs and the typical QSOs in Table 8 and Table 9, respectively.

Table 8
Brightness Variabilities and Color Variabilities of the Red QSOs

Name	$m_{3000\ \text{Å}}-m_{4000\ \text{Å}}$	$\sigma_{g_{P1}}$	$\sigma_{r_{P1}}$	$\sigma_{i_{P1}}$	$\sigma_{z_{P1}}$	$\sigma_{g_{P1}-r_{P1}}$	$\sigma_{r_{P1}-i_{P1}}$	$\sigma_{i_{P1}-z_{P1}}$
SDSS J083732.19+450139.7	−0.274	0.088	0.076	0.076	0.075	0.020	0.017	0.012
SDSS J095823.73+011235.7	−0.278	0.173	0.108	0.098	0.091	0.068	0.049	0.056
SDSS J095915.20+031617.4	−0.135	0.069	0.061	0.064	0.063	0.012	0.027	0.041
SDSS J100027.43+025951.3	−0.049	0.146	0.122	0.103	0.088	0.025	0.022	0.032
SDSS J100043.13+020637.2	−0.098	0.060	0.034	0.032	0.035	0.029	0.015	0.024
SDSS J221110.98−000953.3	−0.112	0.020	0.033	0.030	0.026	0.000	0.017	0.010
SDSS J221155.73−001043.9	−0.186	0.053	0.052	0.058	0.058	0.024	0.040	0.051
SDSS J221317.02+003714.1	−0.310	0.181	0.179	0.114	0.105	0.033	0.077	0.068
SDSS J221337.66−002017.5	−0.237	0.149	0.124	0.112	0.100	0.039	0.019	0.018
SDSS J221348.77−005007.8	−0.322	0.159	0.133	0.112	0.114	0.042	0.039	0.057
SDSS J221356.01−002455.7	−0.187	0.105	0.093	0.089	0.091	0.023	0.012	0.029
SDSS J221412.45−001009.7	0.121	0.069	0.052	0.050	0.057	0.037	0.027	0.025
SDSS J221424.68−005221.7	−0.044	0.248	0.150	0.107	0.083	0.116	0.064	0.051
SDSS J221449.38+011525.3	0.119	0.141	0.092	0.058	0.041	0.079	0.060	0.031
SDSS J221512.15−005152.5	−0.034	0.104	0.070	0.035	0.030	0.050	0.029	0.000
SDSS J221707.16−004721.9	−0.167	0.154	0.144	0.122	0.106	0.025	0.038	0.035
SDSS J221712.61−002502.8	−0.130	0.231	0.193	0.131	0.132	0.058	0.086	0.059
SDSS J221715.18+002615.0	0.007	0.235	0.214	0.116	0.090	0.000	0.093	0.011
SDSS J221715.70+005630.2	−0.228	0.062	0.044	0.045	0.042	0.039	0.023	0.000
SDSS J221750.50−002425.9	−0.314	0.097	0.091	0.083	0.075	0.027	0.030	0.039
SDSS J221826.14+000012.8	−0.139	0.147	0.102	0.076	0.076	0.067	0.038	0.042
SDSS J221907.95+004023.3	0.117	0.122	0.085	0.063	0.069	0.042	0.032	0.043
SDSS J221917.01−000757.5	−0.203	0.073	0.059	0.055	0.060	0.031	0.027	0.033
SDSS J221932.17−004551.9	0.079	0.068	0.068	0.068	0.067	0.025	0.025	0.032
SDSS J221956.75+005913.3	0.078	0.100	0.031	0.031	0.016	0.064	0.031	0.000
SDSS J222000.58+010742.1	0.124	0.172	0.088	0.058	0.056	0.090	0.041	0.014
SDSS J222133.75+010119.2	−0.186	0.179	0.139	0.117	0.105	0.042	0.022	0.009
SDSS J232458.66−000302.9	0.156	0.083	0.069	0.065	0.076	0.014	0.022	0.022
SDSS J232545.18−004309.1	−0.311	0.137	0.122	0.070	0.059	0.048	0.060	0.008
SDSS J232710.78+001703.7	−0.328	0.065	0.049	0.042	0.033	0.009	0.014	0.022
SDSS J232712.98−003618.3	−0.199	0.113	0.087	0.072	0.067	0.030	0.039	0.036
SDSS J232801.47+001705.0	−0.316	0.199	0.133	0.091	0.096	0.065	0.063	0.042
SDSS J232953.52+005106.6	−0.226	0.224	0.152	0.083	0.084	0.089	0.061	0.000
SDSS J233129.83−004933.2	0.322	0.122	0.124	0.108	0.132	0.005	0.028	0.020

Note. Name: object name; $m_{4000\ \text{Å}}-m_{3000\ \text{Å}}$: magnitude difference between 3000 and 4000 Å; $\sigma_{g_{P1}}$, $\sigma_{r_{P1}}$, $\sigma_{i_{P1}}$, and $\sigma_{z_{P1}}$: BVAs in g_{P1}, r_{P1}, i_{P1}, and z_{P1} bands; $\sigma_{g_{P1}-r_{P1}}$, $\sigma_{r_{P1}-i_{P1}}$, and $\sigma_{i_{P1}-z_{P1}}$: CVAs in $g_{P1}-r_{P1}$, $r_{P1}-i_{P1}$, and $i_{P1}-z_{P1}$ colors.

Table 9
Same as Table 8, but for the Typical QSOs

Name	$m_{3000\,\text{Å}} - m_{3000\,\text{Å}}$	σ_{gP1}	σ_{rP1}	σ_{iP1}	σ_{zP1}	$\sigma_{gP1-rP1}$	$\sigma_{rP1-iP1}$	$\sigma_{iP1-zP1}$
SDSS J083924.96+442106.0	−0.720	0.083	0.066	0.064	0.064	0.015	0.009	0.010
SDSS J083950.19+432941.3	−0.654	0.128	0.120	0.094	0.086	0.017	0.023	0.015
SDSS J084101.70+425806.4	−0.748	0.178	0.195	0.193	0.174	0.016	0.005	0.006
SDSS J084140.62+434908.5	−0.751	0.087	0.064	0.060	0.053	0.026	0.011	0.012
SDSS J084146.01+450443.4	−0.722	0.182	0.143	0.142	0.140	0.032	0.010	0.031
SDSS J084153.02+443157.0	−0.693	0.173	0.166	0.151	0.124	0.014	0.025	0.028
SDSS J084221.84+453516.2	−0.769	0.115	0.116	0.109	0.091	0.007	0.030	0.033
SDSS J084512.98+445209.0	−0.671	0.080	0.066	0.072	0.062	0.024	0.012	0.017
SDSS J095530.55+021652.8	−0.738	0.127	0.112	0.112	0.093	0.012	0.027	0.039
SDSS J095642.33+020554.4	−0.738	0.145	0.110	0.126	0.125	0.008	0.000	0.000
SDSS J095656.19+021315.1	−0.589	0.112	0.104	0.110	0.101	0.012	0.012	0.000
SDSS J095705.13+014949.5	−0.583	0.211	0.178	0.145	0.170	0.052	0.027	0.030
SDSS J095819.87+022903.4	−0.772	0.197	0.119	0.080	0.073	0.070	0.046	0.019
SDSS J095945.61+013032.1	−0.786	0.116	0.089	0.086	0.101	0.019	0.006	0.023
SDSS J095946.01+024743.5	−0.778	0.157	0.104	0.119	0.111	0.040	0.012	0.015
SDSS J100025.24+015852.0	−0.778	0.148	0.134	0.129	0.096	0.016	0.012	0.049
SDSS J100104.86+011421.2	−0.743	0.045	0.050	0.053	0.050	0.000	0.000	0.000
SDSS J100106.38+030309.8	−0.742	0.297	0.302	0.220	0.218	0.019	0.060	0.038
SDSS J100119.69+010501.7	−0.689	0.072	0.048	0.046	0.048	0.018	0.010	0.016
SDSS J100125.46+005205.5	−0.721	0.121	0.124	0.124	0.094	0.015	0.029	0.049
SDSS J100210.72+023026.1	−0.602	0.073	0.072	0.083	0.077	0.021	0.016	0.010
SDSS J100226.98+033039.7	−0.594	0.097	0.110	0.105	0.094	0.020	0.016	0.012
SDSS J100229.01+010858.4	−0.738	0.101	0.102	0.085	0.087	0.011	0.017	0.019
SDSS J100232.13+023537.3	−0.626	0.198	0.173	0.148	0.113	0.037	0.050	0.067
SDSS J100324.56+021831.3	−0.664	0.098	0.086	0.069	0.078	0.014	0.024	0.028
SDSS J100327.67+015742.3	−0.597	0.101	0.082	0.086	0.087	0.020	0.007	0.010
SDSS J100333.99+024126.2	−0.632	0.093	0.064	0.058	0.046	0.030	0.008	0.017
SDSS J100421.01+013647.3	−0.618	0.095	0.077	0.073	0.070	0.020	0.008	0.011
SDSS J100429.00+025209.2	−0.761	0.172	0.161	0.148	0.141	0.012	0.010	0.017
SDSS J104239.65+583230.9	−0.756	0.085	0.077	0.071	0.062	0.018	0.013	0.006
SDSS J104405.38+570024.2	−0.715	0.101	0.080	0.062	0.065	0.025	0.034	0.047
SDSS J104556.84+570747.0	−0.756	0.119	0.120	0.108	0.109	0.031	0.052	0.087
SDSS J104625.02+584839.1	−0.733	0.171	0.142	0.127	0.116	0.011	0.019	0.000
SDSS J104633.70+571530.4	−0.766	0.132	0.127	0.112	0.105	0.007	0.029	0.029
SDSS J104659.37+573055.8	−0.758	0.293	0.235	0.301	0.274	0.046	0.040	0.030
SDSS J104757.52+573451.8	−0.704	0.272	0.240	0.217	0.195	0.057	0.017	0.022
SDSS J104859.67+565648.6	−0.746	0.077	0.066	0.065	0.063	0.021	0.012	0.010
SDSS J105000.21+581904.2	−0.688	0.075	0.064	0.068	0.056	0.006	0.010	0.012
SDSS J105141.16+591305.2	−0.590	0.243	0.126	0.079	0.085	0.120	0.065	0.046
SDSS J105239.60+572431.3	−0.661	0.052	0.037	0.041	0.034	0.024	0.013	0.010
SDSS J121440.10+473226.2	−0.733	0.107	0.095	0.097	0.081	0.026	0.013	0.015
SDSS J121729.40+471424.8	−0.615	0.039	0.030	0.029	0.026	0.008	0.008	0.015
SDSS J121934.41+465155.4	−0.650	0.142	0.122	0.097	0.083	0.020	0.029	0.029
SDSS J121946.40+473748.1	−0.760	0.176	0.177	0.160	0.144	0.015	0.025	0.023
SDSS J122025.31+480531.3	−0.710	0.059	0.070	0.061	0.064	0.023	0.021	0.027
SDSS J122046.61+464347.4	−0.580	0.091	0.095	0.103	0.082	0.014	0.009	0.018
SDSS J122107.54+462736.0	−0.768	0.157	0.177	0.144	0.111	0.021	0.035	0.026
SDSS J122302.22+482036.0	−0.654	0.209	0.196	0.148	0.144	0.029	0.039	0.025
SDSS J122419.76+481104.2	−0.666	0.095	0.083	0.075	0.070	0.017	0.000	0.000
SDSS J122517.84+461126.8	−0.703	0.126	0.110	0.107	0.105	0.019	0.018	0.028
SDSS J122607.92+473700.5	−0.763	0.130	0.112	0.113	0.108	0.024	0.014	0.020
SDSS J141154.12+520023.4	−0.628	0.067	0.062	0.049	0.038	0.020	0.019	0.017
SDSS J141226.48+525347.6	−0.697	0.087	0.080	0.096	0.088	0.022	0.014	0.012
SDSS J141318.96+543202.4	−0.748	0.139	0.084	0.062	0.060	0.038	0.026	0.000
SDSS J141352.98+523444.2	−0.758	0.090	0.085	0.065	0.058	0.005	0.020	0.021
SDSS J141500.38+520658.5	−0.748	0.086	0.092	0.088	0.089	0.034	0.057	0.066
SDSS J141533.89+520558.0	−0.782	0.165	0.133	0.119	0.108	0.031	0.012	0.022
SBS 1415+541	−0.637	0.083	0.091	0.087	0.068	0.017	0.017	0.027
SDSS J141856.19+535845.0	−0.648	0.078	0.060	0.056	0.046	0.021	0.008	0.013
SDSS J142008.28+521646.8	−0.776	0.055	0.043	0.038	0.036	0.020	0.012	0.007
SDSS J142052.43+525622.4	−0.743	0.119	0.124	0.124	0.114	0.017	0.013	0.018
SDSS J160523.10+545613.3	−0.756	0.065	0.058	0.052	0.060	0.011	0.015	0.018
SDSS J160630.60+542007.5	−0.736	0.077	0.079	0.093	0.082	0.016	0.018	0.024
SDSS J221115.06−000030.9	−0.567	0.207	0.185	0.153	0.170	0.065	0.079	0.089

Table 9

(Continued)

Name	$m_{3000\,\text{Å}} - m_{3000\,\text{Å}}$	$\sigma_{g_{P1}}$	$\sigma_{r_{P1}}$	$\sigma_{i_{P1}}$	$\sigma_{z_{P1}}$	$\sigma_{g_{P1}-r_{P1}}$	$\sigma_{r_{P1}-i_{P1}}$	$\sigma_{i_{P1}-z_{P1}}$
SDSS J221203.19+000239.0	−0.624	0.142	0.094	0.126	0.093	0.057	0.018	0.026
SDSS J221301.63+004342.7	−0.613	0.100	0.079	0.078	0.074	0.032	0.010	0.014
SDSS J221337.97−004305.9	−0.578	0.048	0.038	0.037	0.035	0.014	0.008	0.008
SDSS J221407.38+000727.1	−0.664	0.087	0.072	0.084	0.077	0.019	0.018	0.029
SDSS J221447.74−002032.6	−0.607	0.065	0.050	0.065	0.059	0.018	0.011	0.010
SDSS J221619.25−002430.4	−0.618	0.187	0.229	0.216	0.177	0.050	0.038	0.047
SDSS J221708.83+002717.1	−0.701	0.071	0.074	0.072	0.075	0.017	0.011	0.011
SDSS J221756.92+010119.5	−0.662	0.037	0.037	0.035	0.032	0.005	0.009	0.005
SDSS J221901.87+000025.9	−0.665	0.068	0.062	0.060	0.057	0.012	0.004	0.000
SDSS J221912.12+003612.9	−0.664	0.075	0.081	0.074	0.067	0.005	0.011	0.015
SDSS J222029.54+004401.3	−0.600	0.057	0.053	0.045	0.059	0.013	0.021	0.016
SDSS J222036.80−002051.9	−0.627	0.250	0.222	0.267	0.227	0.049	0.039	0.021
SDSS J222123.28−001824.1	−0.589	0.062	0.054	0.049	0.041	0.011	0.008	0.009
SDSS J222147.92−002205.8	−0.613	0.102	0.090	0.087	0.078	0.024	0.017	0.016
SDSS J232355.04−001507.3	−0.676	0.067	0.049	0.053	0.045	0.026	0.038	0.043
SDSS J232423.68−002320.6	−0.768	0.084	0.078	0.061	0.060	0.026	0.020	0.000
SDSS J232428.36−005244.3	−0.618	0.158	0.120	0.074	0.054	0.043	0.033	0.038
SDSS J232500.55−011445.0	−0.719	0.095	0.095	0.096	0.088	0.001	0.008	0.019
SDSS J232515.93+002229.1	−0.669	0.044	0.042	0.041	0.031	0.018	0.010	0.012
SDSS J232525.32+000352.1	−0.676	0.117	0.096	0.108	0.089	0.030	0.049	0.051
SDSS J232525.52+001136.8	−0.684	0.091	0.081	0.080	0.083	0.022	0.009	0.010
SDSS J232554.37−001823.8	−0.623	0.037	0.040	0.029	0.022	0.035	0.026	0.021
SDSS J232555.33+004109.9	−0.655	0.153	0.127	0.129	0.123	0.036	0.012	0.029
SDSS J232626.14+000922.2	−0.753	0.106	0.090	0.084	0.076	0.025	0.011	0.022
SDSS J232705.65−000648.5	−0.615	0.314	0.329	0.335	0.257	0.050	0.017	0.063
SDSS J232712.41−001815.7	−0.660	0.150	0.126	0.126	0.101	0.029	0.013	0.023
SDSS J232728.26+005341.4	−0.657	0.088	0.070	0.068	0.056	0.024	0.016	0.011
SDSS J232742.67+000653.9	−0.593	0.157	0.176	0.155	0.146	0.016	0.028	0.031
SDSS J232743.72+002837.0	−0.617	0.221	0.163	0.105	0.097	0.067	0.060	0.004
SDSS J232757.24−000035.9	−0.751	0.156	0.129	0.131	0.114	0.032	0.022	0.034
SDSS J232757.95−002058.8	−0.742	0.120	0.096	0.109	0.112	0.027	0.017	0.008
SDSS J232803.53−001656.3	−0.596	0.159	0.144	0.091	0.089	0.028	0.047	0.040
SDSS J232825.86+004439.7	−0.702	0.073	0.058	0.058	0.040	0.015	0.012	0.010
SDSS J232833.50−005234.2	−0.593	0.109	0.108	0.092	0.093	0.020	0.048	0.066
SDSS J232928.88−011405.6	−0.581	0.331	0.208	0.112	0.084	0.118	0.102	0.051
SDSS J232930.16−000752.7	−0.642	0.096	0.101	0.095	0.076	0.023	0.019	0.015
SDSS J233007.17−000324.4	−0.605	0.085	0.077	0.074	0.069	0.014	0.015	0.019
SDSS J233010.93−002951.5	−0.711	0.097	0.090	0.070	0.064	0.015	0.019	0.016
SDSS J233011.42−001800.1	−0.600	0.049	0.049	0.049	0.041	0.012	0.009	0.011
SDSS J233020.71+001727.5	−0.669	0.047	0.042	0.035	0.032	0.010	0.007	0.009
SDSS J233023.48+000811.8	−0.744	0.128	0.114	0.126	0.116	0.018	0.008	0.012
SDSS J233027.81−005905.7	−0.685	0.094	0.083	0.076	0.062	0.024	0.007	0.019
SDSS J233029.16+003746.5	−0.739	0.369	0.318	0.250	0.210	0.070	0.116	0.091
SDSS J233119.80−010632.3	−0.707	0.119	0.101	0.097	0.082	0.023	0.015	0.026
SDSS J233133.07−005609.1	−0.774	0.058	0.062	0.047	0.051	0.013	0.025	0.022
SDSS J233138.97−002429.2	−0.775	0.164	0.155	0.161	0.137	0.013	0.030	0.053
SDSS J233139.32−001516.7	−0.774	0.055	0.048	0.049	0.035	0.010	0.022	0.018
SDSS J233149.48+000719.4	−0.685	0.079	0.064	0.063	0.070	0.039	0.047	0.059
SDSS J233155.01−011515.0	−0.600	0.069	0.062	0.054	0.050	0.018	0.016	0.005
SDSS J233157.77−005130.9	−0.714	0.125	0.120	0.093	0.089	0.003	0.020	0.002
SDSS J233229.37+002740.3	−0.684	0.252	0.250	0.203	0.172	0.035	0.071	0.053
SDSS J233230.41+000137.6	−0.571	0.158	0.143	0.116	0.077	0.023	0.041	0.040
SDSS J233315.84−000452.8	−0.724	0.092	0.087	0.074	0.057	0.017	0.022	0.028
SDSS J233325.16−005835.2	−0.729	0.209	0.149	0.170	0.181	0.062	0.041	0.067
SDSS J233329.00−000308.1	−0.711	0.112	0.106	0.103	0.097	0.022	0.023	0.043
SDSS J233330.57−004832.2	−0.705	0.207	0.208	0.165	0.140	0.015	0.021	0.012
SDSS J233409.36−010118.0	−0.667	0.172	0.178	0.184	0.161	0.036	0.040	0.030
SDSS J233411.74−011131.1	−0.583	0.109	0.096	0.087	0.067	0.041	0.020	0.030

ORCID iDs

I-Chenn Chen https://orcid.org/0000-0002-1497-9884
Chorng-Yuan Hwang https://orcid.org/0000-0002-3658-0903
Nick Kaiser https://orcid.org/0000-0001-6511-4306
Eugene A. Magnier https://orcid.org/0000-0002-7965-2815
Nigel Metcalfe https://orcid.org/0000-0001-9034-4402
Christopher Waters https://orcid.org/0000-0003-1989-4879

References

Ai, Y. L., Yuan, W., Zhou, H. Y., et al. 2010, ApJL, 716, L31
Antonucci, R. 1993, ARA&A, 31, 473
Benn, C. R., Vigotti, M., Carballo, R., Gonzalez-Serrano, J. I., & Sánchez, S. F. 1998, MNRAS, 295, 451
Chambers, K. 2011, American Astronomical Society Meeting Abstracts, 218, 113.01
Cristiani, S., Trentini, S., La Franca, F., & Andreani, P. 1997, A&A, 321, 123
Fukugita, M., Ichikawa, T., Gunn, J. E., et al. 1996, AJ, 111, 1748
Fynbo, J. P. U., Krogager, J.-K., Venemans, B., et al. 2013, ApJS, 204, 6
Giveon, U., Maoz, D., Kaspi, S., Netzer, H., & Smith, P. S. 1999, MNRAS, 306, 637
Glikman, E., Gregg, M. D., Lacy, M., et al. 2004, ApJ, 607, 60
Glikman, E., Helfand, D. J., White, R. L., et al. 2007, ApJ, 667, 673
Glikman, E., Urrutia, T., Lacy, M., et al. 2012, ApJ, 757, 51
Glikman, E., Urrutia, T., Lacy, M., et al. 2013, ApJ, 778, 127
Hall, P. B., Gallagher, S. C., Richards, G. T., et al. 2006, AJ, 132, 1977
Hawkins, M. R. S. 2003, MNRAS, 344, 492
Hodapp, K. W., Kaiser, N., Aussel, H., et al. 2004, AN, 325, 636
Kaiser, N., Aussel, H., Burke, B. E., et al. 2002, Proc. SPIE, 4836, 154
Kaiser, N., Burgett, W., Chambers, K., et al. 2010, Proc. SPIE, 7733, 77330E
Kawaguchi, T., Mineshige, S., Umemura, M., & Turner, E. L. 1998, ApJ, 504, 671
Magnier, E. 2006, in The Advanced Maui Optical and Space Surveillance Technologies Conf., ed. D. B. Ryan (Maui, HI: Maui Economic Development Board), 50
Magnier, E. 2007, in ASP Conf. Ser. 364, The Future of Photometric, Spectrophotometric and Polarimetric Standardization, ed. C. Sterken (San Francisco, CA: ASP), 153
Magnier, E. A., Liu, M., Monet, D. G., & Chambers, K. C. 2008, in IAU Symp. 248, A Giant Step: From Milli- to Micro-arcsecond Astrometry, ed. W. J. Jin, I. Platais, & M. A. C. Perryman (Paris: IAU), 553
Magnier, E. A., Schlafly, E., Finkbeiner, D., et al. 2013, ApJS, 205, 20
Malkan, M. A., & Sargent, W. L. W. 1982, ApJ, 254, 22
Matthews, T. A., & Sandage, A. R. 1963, ApJ, 138, 30
Oke, J. B., & Gunn, J. E. 1983, ApJ, 266, 713
Pei, Y. C. 1992, ApJ, 395, 130
Pereyra, N. A., Vanden Berk, D. E., Turnshek, D. A., et al. 2006, ApJ, 642, 87
Rees, M. J. 1984, ARA&A, 22, 471
Richards, G. T., Hall, P. B., Vanden Berk, D. E., et al. 2003, AJ, 126, 1131
Sakata, Y., Morokuma, T., Minezaki, T., et al. 2011, ApJ, 731, 50
Sanders, D. B., Soifer, B. T., Elias, J. H., et al. 1988, ApJ, 325, 74
Schlafly, E. F., Finkbeiner, D. P., Jurić, M., et al. 2012, ApJ, 756, 158
Schmidt, K. B., Rix, H.-W., Shields, J. C., et al. 2012, ApJ, 744, 147
Schmidt, M. 1963, Natur, 197, 1040
Schneider, D. P., Richards, G. T., Hall, P. B., et al. 2010, AJ, 139, 2360
Shields, G. A. 1978, Natur, 272, 706
Sun, Y.-H., Wang, J.-X., Chen, X.-Y., & Zheng, Z.-Y. 2014, ApJ, 792, 54
Tonry, J. L., Stubbs, C. W., Lykke, K. R., et al. 2012, ApJ, 750, 99
Ulrich, M.-H., Maraschi, L., & Urry, C. M. 1997, ARA&A, 35, 445
Urrutia, T., Becker, R. H., White, R. L., et al. 2009, ApJ, 698, 1095
Urry, C. M., & Padovani, P. 1995, PASP, 107, 803
Vanden Berk, D. E., Richards, G. T., Bauer, A., et al. 2001, AJ, 122, 549
Vanden Berk, D. E., Wilhite, B. C., Kron, R. G., et al. 2004, ApJ, 601, 692
Walcher, J., Groves, B., Budavári, T., & Dale, D. 2011, Ap&SS, 331, 1
Webster, R. L., Francis, P. J., Petersont, B. A., Drinkwater, M. J., & Masci, F. J. 1995, Natur, 375, 469
Whiting, M. T., Webster, R. L., & Francis, P. J. 2001, MNRAS, 323, 718
Wilhite, B. C., Vanden Berk, D. E., Kron, R. G., et al. 2005, ApJ, 633, 638
Wills, B. J., Netzer, H., & Wills, D. 1985, ApJ, 288, 94
Yip, C. W., Connolly, A. J., Vanden Berk, D. E., et al. 2009, AJ, 137, 5120
Young, M., Elvis, M., & Risaliti, G. 2008, ApJ, 688, 128
Zuo, W., Wu, X.-B., Liu, Y.-Q., & Jiao, C.-L. 2012, ApJ, 758, 104